

## Climatological Coastal Jet Collision, Intermediate Water Formation, and the General Circulation of the Red Sea\*

GIDON ESHEL<sup>+</sup> AND NAOMI H. NAIK

*Lamont-Doherty Earth Observatory, Columbia University, Palisades, New York*

(Manuscript received 5 May 1996, in final form 18 November 1996)

### ABSTRACT

The authors present climatologies of a numerical model of the Red Sea, focusing on the dynamics of winter intermediate water formation. Northward flowing boundary currents are identified as the major dynamical elements. At the northern boundary, the eastern current follows the geometry, eventually turning back to the south. At  $\sim 26^{\circ}\text{N}$  and the western wall the two boundary currents collide. At the collision site, the denser eastern current subducts under the western boundary current. The subduction forces the western boundary current eastward into the interior. Convection communicates the surface fluxes to the downwelled plume and intermediate water forms. The estimated rate, 0.11 Sv ( $\text{Sv} \equiv 10^6 \text{ m}^3 \text{ s}^{-1}$ ), agrees with previous estimates. The authors identify basin-scale sea-surface tilt to the north due to variable thermohaline forcings as the key dynamical variable. The resultant geostrophic eastward cross-channel flow interacts with the boundaries and creates upwelling and surface topography spatial patterns that drive the coastal jets. Upwelling-induced vortex stretching dominates the vorticity balance and governs the separation of the western boundary current from the western wall. The process ceases in the summer.

### 1. Introduction

The Red Sea (RS) presents a unique combination; it is relatively small and has fairly simple geometry, yet it presents many of the same issues as the global ocean. These include the role of convective and subductive water mass formation in maintaining meridional thermohaline overturning, air-sea interactions leading to formation events, interactions with adjacent semienclosed basins, and the significance of small-scale mixing processes.

While increasingly studied in recent years, the understanding of the RS circulation remains unsatisfactory. This is true for issues of the deep circulation (the modes, driving forces, and areas of formation of RS deep, intermediate, and subsurface waters), as well as for interactions of the wind and density driven circulations. Eshel (1996) provides a thorough review of RS climatologies, forcings, and related issues and discusses in some length the World Ocean-RS analogy.

Motivated by the possibility of using the RS as a natural laboratory for global processes and by interest in the

basin itself, in Eshel et al. (1994, hereafter ECB) we constructed a simple inverse box model to analyze hydrographic and  $^3\text{He}$  data from the RS. The inversion results, summarized schematically in Fig. 13 of ECB, provide a zero-order estimate of the RS circulation. These results have some obvious limitations. The model geometry is 2D and coarse. The time dependence is limited to two seasonal solutions, as well as a better constrained annual mean. Perhaps most importantly, the box model is constrained by mass conservation only, potentially giving rise to dynamically inconsistent solutions.

In order to overcome the box model limitations, in this paper we use an OGCM to simulate the climatological seasonal cycle of the RS circulation. Because we are primarily interested in water mass formation, we focus on the winter. We provide a simple unifying dynamical framework for the large-scale motions in the Red Sea. We distinguish between the northern Red Sea, which is dominated by sea surface tilt, and the southern basin, where the wind is more dominant. The main dynamical features in the northern Red Sea are two boundary currents. We interpret them as a quasigeostrophic response to the large-scale pressure gradient to the north, which results from the sea surface tilt. We also advance simple vorticity arguments to explain the termination of the northern, eastern, and western boundary currents at the western boundary around  $26^{\circ}\text{N}$ .

### 2. The model

We employ a 3D, primitive equation OGCM, which has evolved from the Gent and Cane (1989) model (cf.

\*Lamont-Doherty Earth Observatory Contribution Number 5581.

<sup>+</sup>Current affiliation: Center for Earth and Planetary Physics, Harvard University, Cambridge, Massachusetts.

*Corresponding author address:* Dr. Gidon Eshel, Center for Earth and Planetary Physics, Harvard University, Pierce Hall, 29 Oxford Street, Cambridge, MA 01238.  
E-mail: gidon@psyche.harvard.edu

Chen et al. 1994; Murtugudde 1993). Here we run in a rigid-lid mode with a fixed depth of 1500 m. The water column is divided into 14  $z$  levels centered at 10, 35, 65, 100, 145, 200, 265, 340, 425, 520, 670, 870, 1095, and 1360 m. The coastline configuration is realistic. In the south the domain extends southeast of the Bab el Mandeb Strait to include the western part the Gulf of Aden. This permits the model to determine the fluxes across the strait and eliminates the need to specify them.

Time integration uses a Lorenz 4-cycle, with a time step of 0.8 h. A sixth-order Shapiro filter damps high spatial frequencies, with reduced order (higher effective viscosity) near boundaries. Static stability is maintained by a simple one-pass convective adjustment scheme, which is applied three times per day. In addition, there is explicit background vertical mixing of all properties, which is a linear function of property vertical gradients, and a Richardson-number-dependent mixing (Chen et al. 1994). Density varies nonlinearly with temperature, salinity, and pressure according to a 12-term polynomial fit to data (Basin and Reverdin 1992).

The spatial resolution is  $0.125^\circ$ , or  $\sim 12$  km. After experimenting with various spatial resolutions, we found this resolution to adequately represent the domain (reducing it to  $0.05^\circ$  leaves the results essentially unchanged), while keeping the computational burden manageable. Specified initial temperature and salinity are taken from the data described in ECB. In addition to no normal flow, we impose no-slip momentum boundary conditions. This parameterizes the damping effect of the highly irregular coastline, which is dominated by coral reefs with grid-scale features. For temperature and salinity we impose zero flux horizontal boundary conditions.

Because of the much shorter timescales of the barotropic mode, we split it from the baroclinic motions. In order to avoid the prohibitively small time step that will be dictated by the CFL condition, we solve for the barotropic flow only once a day, using an implicit scheme based on the high-order discretization method discussed in Naik et al. (1995).

Since deep-water formation and upper-ocean processes are of prime interest, sea surface temperature and salinity are key variables. We would like to allow the ocean model as much freedom as possible to determine its surface fields and fluxes; specifying them will eliminate a principal degree of freedom from the system. Further, the narrowness of the Red Sea, along with the extreme heat and dryness of the surrounding land masses, create a boundary layer that is often far from equilibrium with the underlying ocean (cf. section 6.) We thus use an advective planetary boundary layer (PBL) model (Seager et al. 1995; Murtugudde et al. 1996) to calculate the heat and buoyancy surface fluxes.

The most attractive feature of the PBL formulation for modeling the Red Sea is that both air temperature and humidity (and, by implication, latent, sensible, and freshwater surface fluxes) are determined internally by

the model, without assuming a local (one-dimensional) equilibrium. The air temperature and humidity calculations are based on observed coastal boundary values [climatologies of the ECMWF analyses (Trenberth 1992)], observed winds [da Silva et al. 1994] plotted in Eshel 1996 (Fig. 1.1)], and calculated surface fluxes. This allows the surface fluxes and the SST to interact relatively freely, as they do in nature. The boundary layer budgets are closed by taking the virtual potential temperature flux into the PBL from the overlying free atmosphere to be a fixed fraction of its surface flux value. Finally, solar fluxes are taken from the Earth Radiation Budget Experiment data (Li and Leighton 1993), and longwave cooling is calculated using a standard bulk formula, calculated SSTs, and da Silva et al.'s (1994) observed cloudiness.

The simulation begins from a state of rest and climatological hydrographic fields. Throughout the run, the planetary boundary layer governs the sea surface temperature and salinity evolution. The input monthly climatologies (of solar radiation, cloud cover, wind stress, air temperature, and humidity) repeat cyclically every 12 months and generate the model's seasonal cycle. North of  $27.6^\circ\text{N}$  and south of the Bab el Mandeb Strait, in addition to the free-surface flux calculations we also relax the model hydrography to climatological values (which also repeat every 12 months, further contributing to a realistic seasonal cycle). The relaxation time constant decreases linearly from the above latitudes toward the respective ends of the domain (i.e., from  $27.6^\circ\text{N}$  to the northern end and from the strait to the southern end), reaching  $\sim 20$  days at the end points. In the Gulf of Aden, this accounts for the input of relatively cool and fresh water into the Red Sea. This effective removal of heat and salt is required for realistic closure of the respective budgets. It also improves the simulation near the strait. At the northern end, inside the adjacent gulfs, the relaxation is needed in order to overcome the restrictions imposed by the lack of bathymetry. In both gulfs, but especially in the Gulf of Suez, the water shallowness dominates surface variability and no reliable simulation can be expected.

To obtain climatologies, we first spin up the model for 25 years. Starting at the 26th year, we save semi-annual mean fields centered at February and August for 15 more years. We define seasonal climatologies as the means of the 15 available seasons.

### 3. Winter upper-layer conditions

The numerical results show a northward upper-layer transport that diminishes to the north. This generally agrees with ECB's estimate, as Table 1 shows. The magnitude at the extreme north is an exception: the numerical estimate is about half of ECB's. While the discrepancy is probably within the uncertainty, we note that the mean location of the casts upon which ECB's results are based is  $27.41^\circ\text{N}$ ,  $34.54^\circ\text{E}$ . Figure 1 shows

TABLE 1. Comparison between the width- and vertical-mean upper-layer winter transports in the numerical results and ECB (in Sv).

Latitude	ECB	Numerical model
13.5°N	0.42	0.46
18.2°N	0.40	0.32
27.0°N	0.19	0.08

that this location is at the downstream extension of an intense northward-flowing eastern boundary current. The hydrography of this point is consistent with the flow intensity of the boundary current. This can yield an overestimated flux in ECB because it omits the western part of the domain where southeastwardly recirculation takes place.

Figure 1 shows surface (upper 20 m) flow and density climatologies. Figure 2 shows the surface (0–40 m) meridional flux, for comparison with ECB’s inversion results. A zero-order prerequisite that the results must satisfy is an adequate simulation of the observed climatological sea surface fields. A comparison of Fig. 3 with observed maps (e.g., ECB and references therein) shows that the results meet this requirement. We will revisit the SST field in the discussion of the boundary layer in section 6. There are three northwestwardly flowing boundary currents in Fig. 1. Near the strait, the inflow from the Gulf of Aden forms an intense, short western boundary current. Near 18°N another western boundary current originates, extending through 25°N. North of 22°N a third boundary current flows to the northwest along the eastern coast all the way to the northern end of the basin. In the extreme north the current follows the northern coast and terminates at the western coast near 26°N.

The fluxes through the strait, shown in Fig. 4, agree reasonably well with observation-based estimates (ECB and references therein); the model inflow is  $\sim 0.39$  Sv ( $\text{Sv} \equiv 10^6 \text{ m}^3 \text{ s}^{-1}$ ), while ECB specified 0.41 Sv. Given this flux (which neglects summer conditions) and mean width and length of 200 and 2000 km, the upper layer of the Red Sea is renewed on a timescale of a few years. In both model and observations, the inflow is confined to the upper 100 m, with outflow below. In the model results the outflow extends from 100 to 350 m, with essentially no flux below. In reality the bottom of the outflow is the strait bottom, which is shallower. The model–data agreement on fluxes through the strait is very important and is not guaranteed beforehand because of the absence of bathymetry and the distorted coastline at the narrow strait region of the model domain. (The latter is dictated by the fourth-order space differencing scheme and the grid configuration; the result is that the model strait is  $\sim 90$  km wide, while in reality it is 55 km.) The outflux amounts to  $\sim 0.25$  Sv, and the density structure [Fig. 4 agrees with observations such as Maillard and Soliman’s (1986) Fig. 12]. Mantyla and Reid (1995) offer a qualitative description

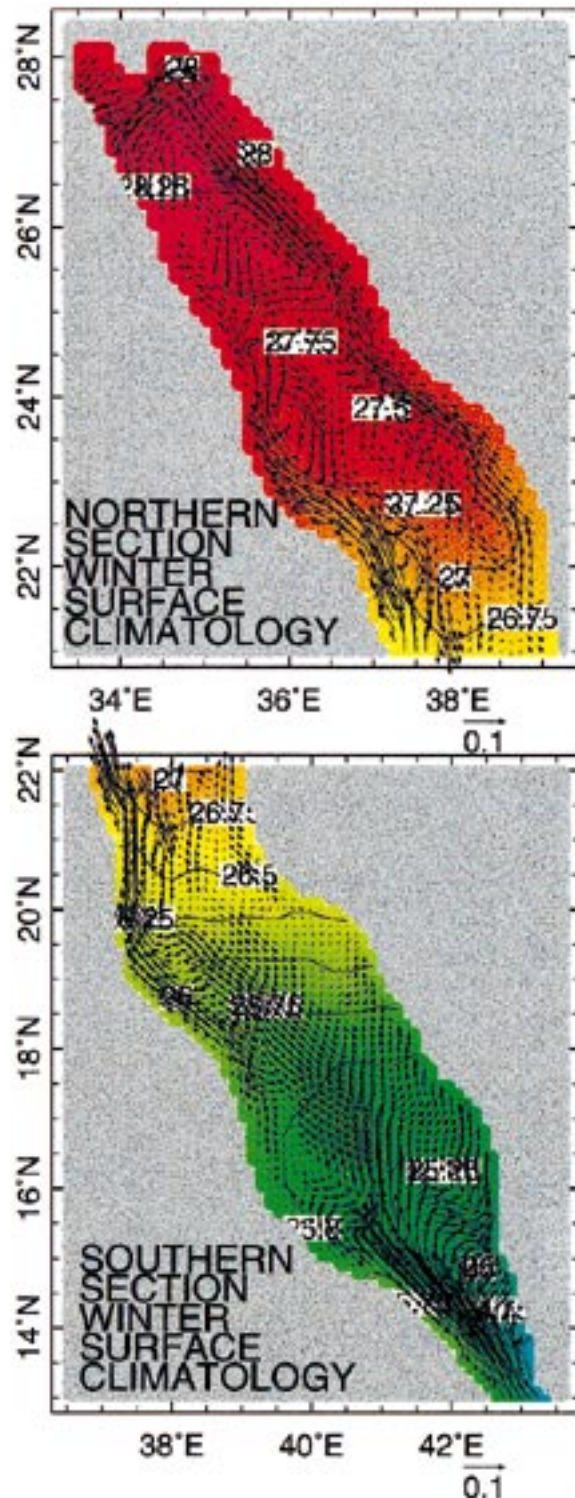


FIG. 1. Model winter climatological upper 20-m density ( $\sigma$ ,  $\text{kg m}^{-3}$ , colors, and contours) and flow. The scale vector ( $\text{m s}^{-1}$ ) and the color scheme are uniform.

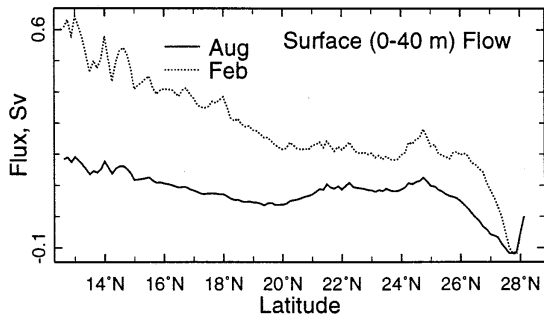


FIG. 2. Calculated semiannual climatological surface meridional flux in Sv.

of the spreading of the high-salinity Red Sea outflow into the Arabian Sea, which is also not at odds with the proposed outflow.

There are two dynamical processes responsible for the inflow through the strait. The first is the most obvious and commonly argued for (e.g., Patzert 1972a,b), namely, the wind stress at the strait region. The winds are confined by land topography to follow the coastline to the northwest. This results in a depressed pycnocline and elevated sea level at the eastern side of the strait compared to the western side (Fig. 4), in geostrophic balance with the inflow. Maillard and Soliman (1986, Fig. 14) clearly show observed temperature distributions across the strait, which support this mechanism. The second dynamical mechanism that drives the inflow is

the winter wind stress over the Gulf of Aden, which is intense and nearly purely easterly. The associated northward Ekman flux raises the sea level along the northern boundary and thus facilitates eastward flow. At the strait, where the northern boundary against which the pressure gradient is built is absent, the easterly wind stress drives the northward inflow through the strait.

During the flow through the strait, the nonlinear zonal relative vorticity advection,  $-u\partial_x\zeta$ , removes vorticity from the bulk of the northward flow due to the boundary-related large negative  $\partial_x\zeta$ . As a result and due to the northward wind stress and pressure gradient, north of the strait the inflow turns anticyclonically to the east. However, this shift is short-lived. Near 16°N the southeasterly winds to the south and the northwesterly winds to the north converge and veer to the west (see the review of Eshel 1996). This results in a positive wind stress curl between 14° and 20°N, with a maximum of  $2 \times 10^{-7} \text{ N m}^{-3}$ . For an upper layer 50 m deep this curl corresponds to  $\partial_x\zeta \approx 4 \times 10^{-12} \text{ s}^{-2}$ . This positive relative vorticity tendency is larger than the opposing negative contribution  $-\beta v \approx -1 \times 10^{-12} \text{ s}^{-2}$  and acts over a much broader area (because the northward flow is narrow). Consequently, a barotropic cyclonic gyre develops between 14° and 20°N, shown in Fig. 5. The boundary friction (due to the no-slip boundary condition) at the western wall where the flow is intensified introduces negative vorticity that partly balances the positive input from the wind. Between 18° and 20°N

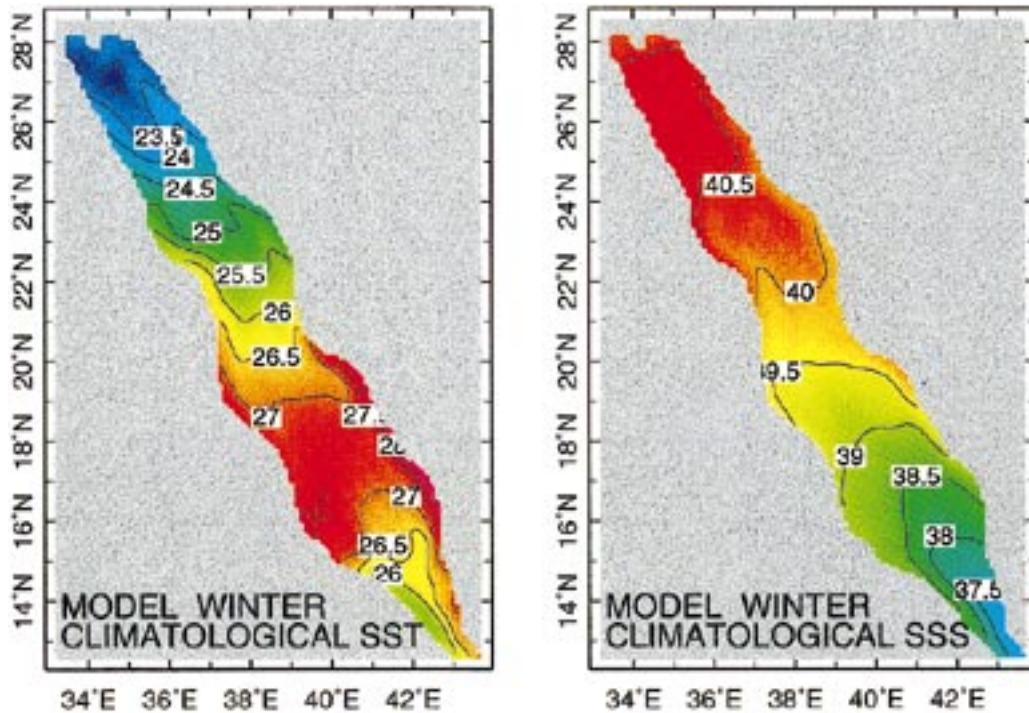


FIG. 3. Calculated winter climatological sea surface fields, °C (left panel), and ‰.

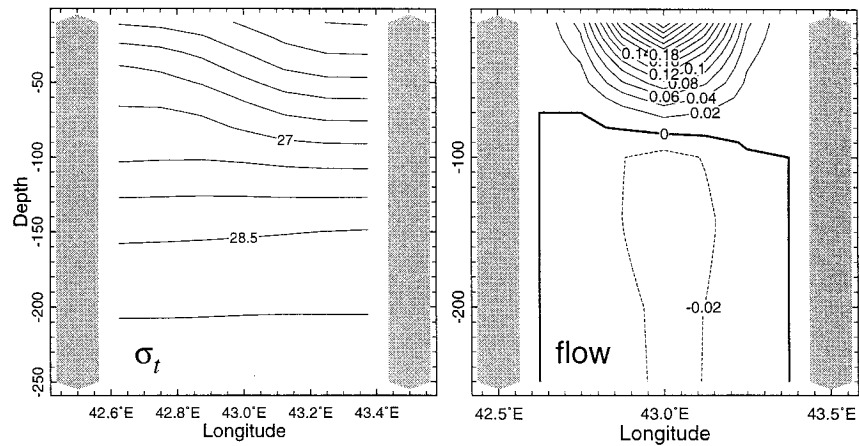


FIG. 4. Model winter climatological density ( $\sigma$ ,  $\text{kg m}^{-3}$ , left panel) and throughflow ( $\text{m s}^{-1}$ , right panel) at the Bab el Mandeb Strait.

the barotropic flow is to the west, so is the Ekman transport due to the northerly winds. Together they drive a  $\sim 0.04 \text{ m s}^{-1}$  westward flow. This flow, along with Rossby waves, which are excited by the adjustment process associated with the wind seasonal cycle, concentrates the flow along the western wall. There the baroclinic speeds far exceed the opposing barotropic ones, and the flow proceeds to the north. North of roughly  $20.5^\circ\text{N}$  the barotropic flow is also to the north but is still negligible compared with the baroclinic upper-layer flow.

The western boundary current sheds small anticyclonic eddies at  $22^\circ$  and  $24^\circ\text{N}$ . Both locations are im-

mediately downstream from coastline features that intrude into the sea. Steering by the coastal geometry creates strong negative  $-\nu\partial_y u$  anomalies slightly upstream from the geometric feature, followed by strong positive  $-\nu\partial_y u$  anomalies immediately downstream from it. This tendency distribution, with eastward accelerations upstream and westward accelerations downstream, generates the anticyclonic eddies as shown schematically in Fig. 6.

Between  $20^\circ$  and  $24^\circ\text{N}$  the western boundary current is the most prominent flow feature, transporting  $\sim 0.35 \text{ Sv}$ . Its maximum speed is  $0.13 \text{ m s}^{-1}$  near  $22^\circ\text{N}$ . Farther north it gradually decays until it terminates at  $26^\circ\text{N}$ .

The northward flowing eastern boundary current originates at  $\sim 21^\circ\text{N}$ . As it flows northwestwardly, it intensifies and deepens, reaching  $0.09 \text{ m s}^{-1}$  and  $>200 \text{ m}$  at  $27^\circ\text{N}$ . Mean velocity, width, and depth of  $0.05 \text{ m s}^{-1}$ ,  $60 \text{ km}$ , and  $150 \text{ m}$  yield a northward flux of  $\sim 0.45 \text{ Sv}$ .

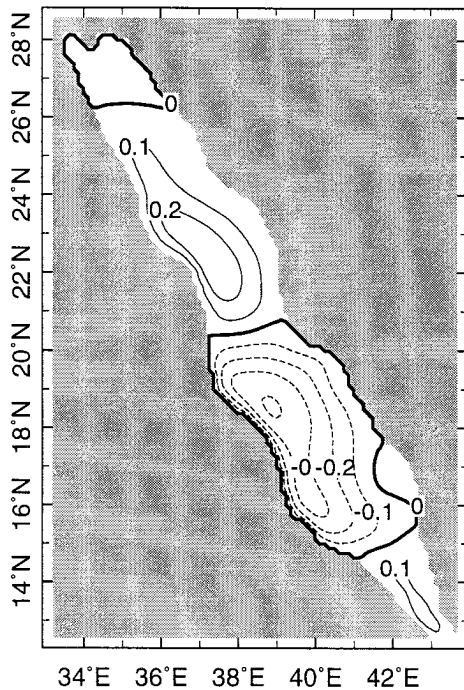


FIG. 5. Model winter climatological barotropic transport streamfunction, Sv.

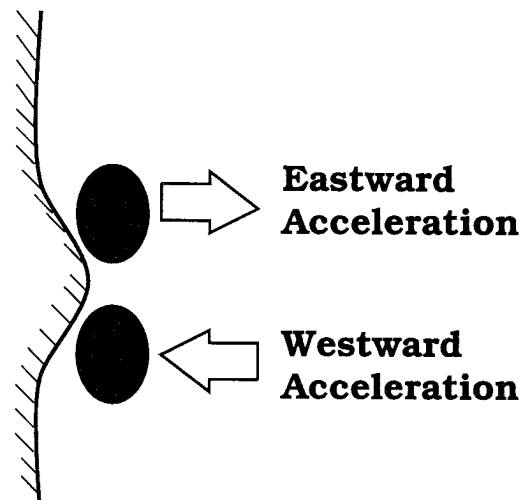


FIG. 6. A schematic of the nonlinear eddy generation process at  $22^\circ$  and  $24^\circ\text{N}$  in winter.

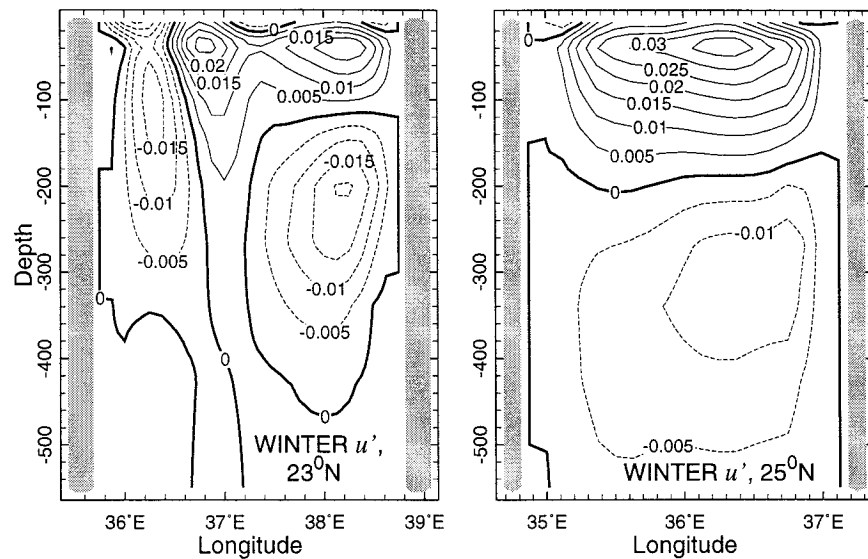


FIG. 7. The cross-channel northeastward flux ( $u' = v \sin 31^\circ + u \cos 31^\circ$ , where  $31^\circ$  is the angle between the principal axis and the north) between the northwardly decaying western boundary current and the northwardly intensifying eastern boundary current.

Most of the downstream intensification is fed by an eastward cross-channel flow (Fig. 7) that is an extension of the northwardly decaying western boundary current. Since the northwesterly winds oppose the cross-channel eastward flow, between  $22^\circ$  and  $26^\circ\text{N}$  its peak intensity is at a depth of 25–30 m. The wind effect is sufficiently reduced over this depth scale ( $\sim$ Ekman depth) to permit pressure gradient dominance.

The eastern boundary current continues, and intensifies, all the way to the northern end. There it turns to the southwest along the northern coast and to the southeast past the Red Sea northwestern corner. In reality, the eastern boundary current interacts with the Gulf of Eilat. Such interactions are largely controlled by topography, which is absent from our model. However, the model retains the bulk effect of the gulf on the Red Sea through the relaxation to observed hydrography at the extreme north. The above results are supported by the few available cross-channel hydrographic sections summarized in Morcos and Soliman (1972). Their calculated dynamic topographies, shown in their Figs. 8a (surface) and 8b (100 m), are strikingly similar to the structures described above. Both figures show an eastern boundary current with a southwestwardly extension and a western boundary current that leaves the coast into the interior around  $26^\circ\text{N}$ . At that west coast point, in both our and Morcos and Soliman's results, the western boundary current collides with the extension of the eastern one. The eastern boundary current terminates there, and the western one loses its boundary current characteristics. We explain this phenomenon below.

All the dynamical features north of  $\sim 18^\circ\text{N}$  can be placed in a simple dynamical framework. The key variable is the large-scale meridional sea surface tilt. While

the sea surface is sloping down toward the north throughout the year, the amplitude of this slope is enhanced in winter. This enhancement is tightly coupled to the seasonal cycle of surface fluxes. Figure 8 shows that while in summer there is a small heat loss throughout most of the Red Sea and an intense heat gain at the extreme north, the winter patterns are almost diametrically opposite. Starting with a  $40 \text{ W m}^{-2}$  loss near  $17^\circ\text{N}$ , the heat loss increases to the north, finally reaching  $\sim 280 \text{ W m}^{-2}$ . The net evaporation (Fig. 8) can potentially add to the formation of dense surface water in the north. While the summer evaporation is higher, it is centered around  $25^\circ\text{N}$  and decreases toward the extreme north. In winter, the net evaporation increases monotonically to the north and peaks at  $>1.9 \text{ m yr}^{-1}$  at the northern end. To compare the contributions of the heat and freshwater fluxes to surface density variability, we calculate the surface buoyancy flux,  $B_0 = B_Q + B_{E-P} = (c_p \rho)^{-1} g \alpha Q + g \beta S (E - P)$ . Here  $g$  and  $c_p$  are the gravitational acceleration and water heat capacity,  $\alpha$  and  $\beta$  are the water thermal and haline contraction coefficients,  $\rho$  and  $S$  are the surface density and salinity, and  $Q$  and  $(E - P)$  are the heat and freshwater fluxes. Here  $B_0$  can be thought of as the surface flux of potential energy  $\rho g z$  per unit mass per unit time. Figure 9 shows the seasonal maps of  $B_Q$  and  $B_{E-P}$ . Evidently, the haline contribution is small. Thus, the heat and freshwater fluxes act together to increase the large-scale pressure gradient in the northern Red Sea in winter, but the haline contribution is secondary.

As a cautionary remark, note that the present model configuration resolves the issue of sea surface tilt only partially. This is because the freshwater surface flux affects surface salinity (as a "virtual salt flux"), but

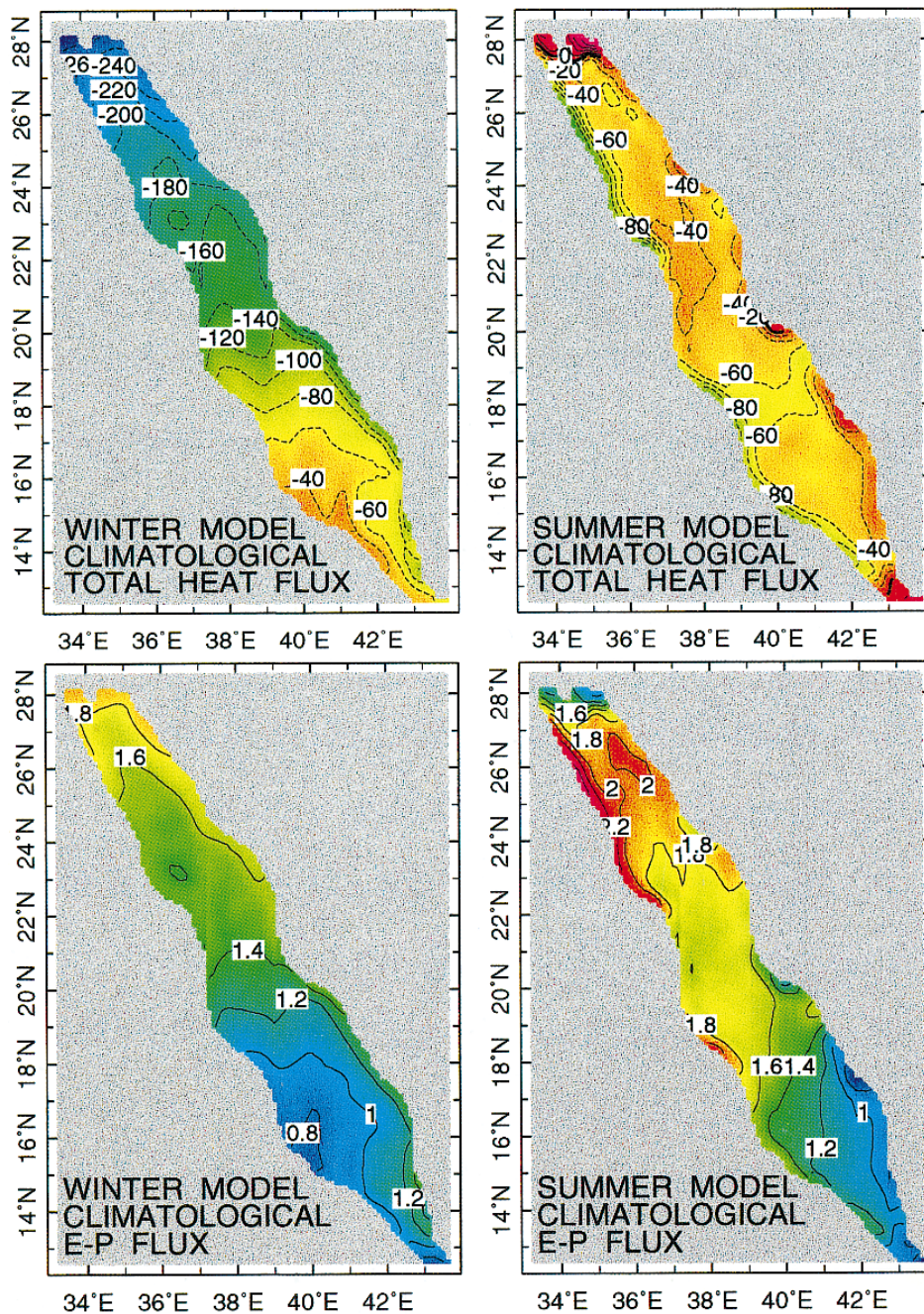


FIG. 8. Model seasonal climatological total surface heat fluxes ( $W m^{-2}$ , upper panels, positive fluxes are defined as heating the surface ocean) and net evaporative freshwater loss from the surface ( $m yr^{-1}$ , lower panels).

cannot affect the total volume, and thus the basin-scale barotropic pressure gradient. Since Fig. 9 shows that the winter buoyancy flux is negative throughout the RS, it is clear that the basin-mean sea surface elevation decreases somewhat to accommodate the necessary replacement inflow. Since in the rigid-lid, flat-bottom configuration the total volume remains fixed, this effect is

absent from the current results. When a free-surface, variable bathymetry version of the model becomes available, we will examine the effect of inclusion of this term. We do not anticipate it will alter the results considerably since it has been shown (e.g., Patzert 1972a,b) that the strait throughflow is mostly baroclinic. Taking 1850 km, 200 km, and 2 m  $yr^{-1}$  as the mean length,

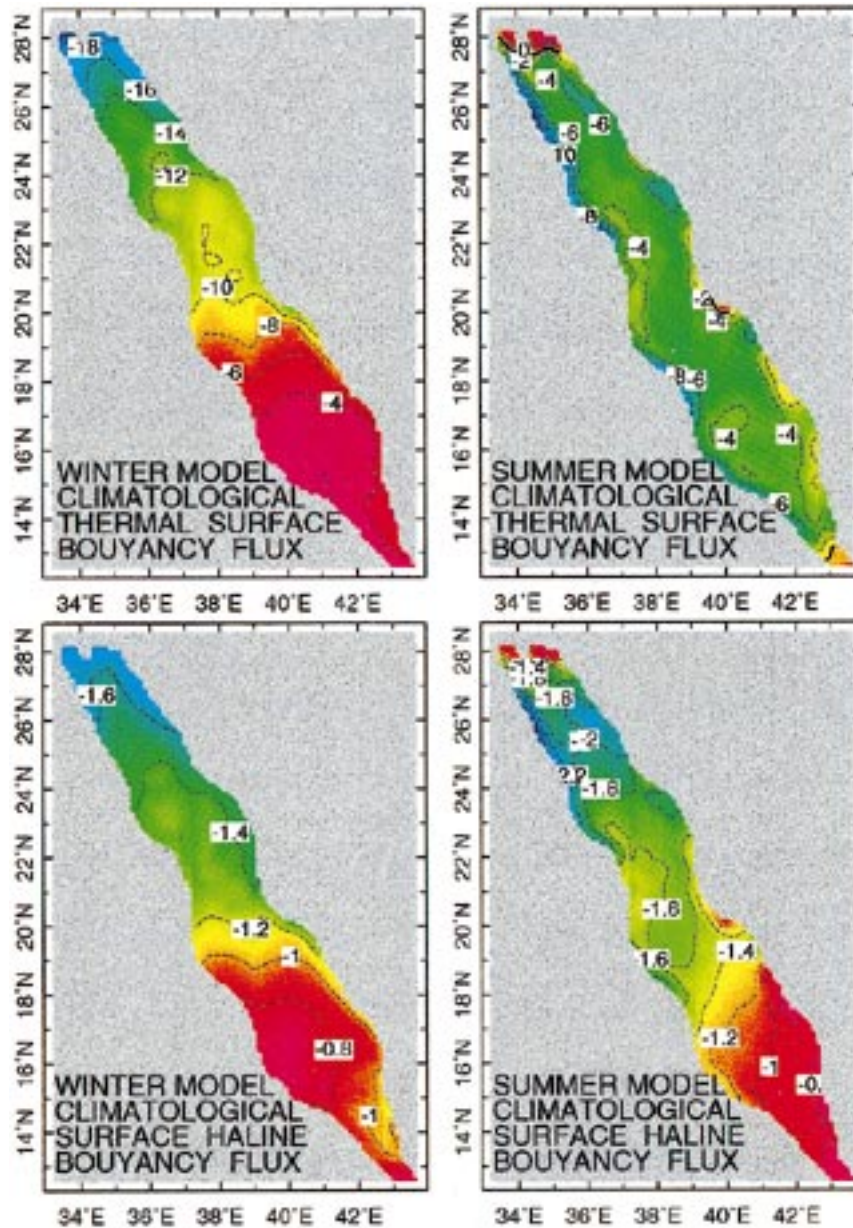


FIG. 9. Thermal (upper panels) and haline climatological surface buoyancy fluxes,  $10^{-8} \text{ m}^2 \text{ s}^{-3}$ .

width, and annual evaporation of the RS, the  $(E - P)$ -driven mean throughflow is  $\sim 0.02 \text{ Sv}$ , or 5% of the total in winter, a reasonably small error. A related issue is the heat and salt fluxes associated with the barotropic strait throughflow, which potentially can completely distort the respective budgets. However, because of the relatively small barotropic throughflow and because the relaxation in the Gulf of Aden fixes the inflow hydrography very nearly climatology throughout the integration, here such errors are small.

The thermohaline surface fluxes create and maintain a surface density gradient in the northern Red Sea,

which is intensified in winter. To quantify this effect, we calculate the ratio of the climatological densities averaged over the upper 200 m and the channel width at  $27^\circ$  and  $21^\circ\text{N}$ . This ratio is 1.0363 in August and 1.0396 in February. It yields a winter increase in dynamic height difference between  $21^\circ$  and  $27^\circ\text{N}$  of 0.33 m. Over the  $\sim 600 \text{ km}$  separating the two points, this translates to a winter northwestward acceleration  $0.94 \text{ m s}^{-1} \text{ day}^{-1}$  higher than the summer one.

The interior cross-channel northeast flow of Fig. 7 is a geostrophic response to the large-scale northward pressure gradient (in section 4 we show that the max-

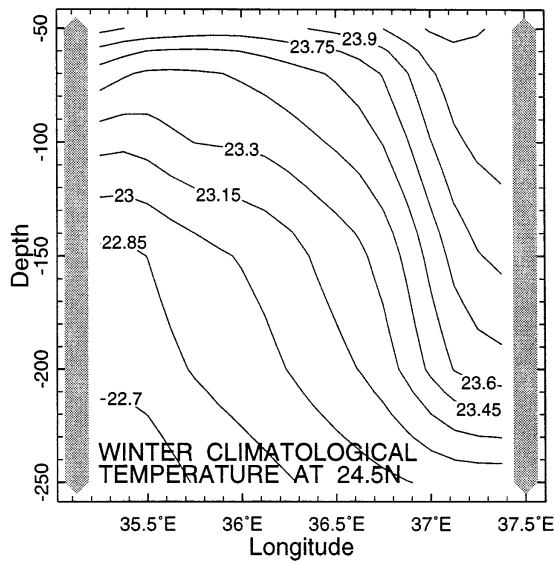


FIG. 10. Model winter climatological temperature cross section at 24.5°N.

imum cross-channel flow coincides with the strongest  $\nabla P$ . A corollary of this interpretation is that the wind forcing in the northern Red Sea is secondary since it would produce cross-channel flow from east to west, opposite to the observed. The cross-channel flow entails surface divergence(convergence) and up(down)welling along the western(eastern) boundaries. The vertical motions displace the isotherms, as is evident in Fig. 10. The situation is represented schematically in Fig. 11. Maillard's (1971) sections across the Red Sea at 21°N (her Fig. 7) are consistent with such a structure. They show elevated isopycnals and isohalines along the western boundary with width scales  $O(20 \text{ km})$ . The sea level displacements at both boundaries drive northward flows, with width scales given by the local baroclinic radius of deformation. Since the latter increases northward in response to the upper-layer deepening, so does the deformation radius. This partly accounts for the computed northward widening of the eastern boundary current.

We now consider the collision and termination of the boundary currents at 26°N near the western boundary. Figure 12 shows that the rate of relative vorticity generation by column stretching is negligible in the interior, but dominates along the northern Red Sea boundaries. At the western side  $w_{-h} > 0$ , so  $\partial_z w < 0$ , while at the eastern boundary  $w_{-h} < 0$  and  $\partial_z w > 0$ . Although  $|\zeta| \approx f$  in the thin frictional layers between the boundary currents and the walls, averaged over the boundary current widths  $|\zeta| \ll f$ ; thus,  $f + \zeta > 0$  on both sides. Vortex stretching generates positive(negative) vorticity along the paths of the eastern(western) boundary currents. The vorticity generation at the eastern wall does not stop at the northern boundary. At the northern coast, the northwesterly wind drives the eastern boundary flow to the southwest past

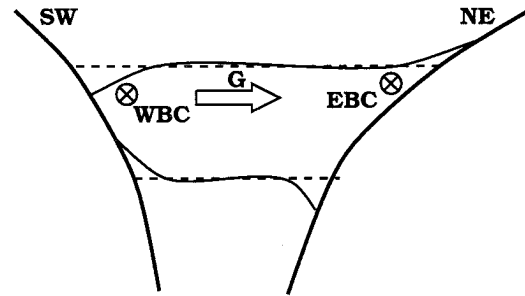


FIG. 11. Schematic of the boundary current dynamics. Here  $G$  is the interior northeastwardly cross-channel flow, in geostrophic balance with the large-scale sea surface slope to the north. **EBC** and **WBC** are the eastern and western boundary currents, both in geostrophic balance with the cross-channel tilts that result from the interactions of the cross-channel flow with the boundaries; **SW** and **NE** are the Red Sea boundaries. As indicated, northward geostrophic flows follow along both boundaries.

the northeast corner of the RS. In the model representation of the Gulfs of Eilat and Suez, this is associated with intense coastal upwelling along the eastern coasts of both. While this is likely to be true, our model geometry is too crude to represent it correctly. In the model, the generation of negative vorticity associated with this upwelling is not enough to stop the cyclonic flow.

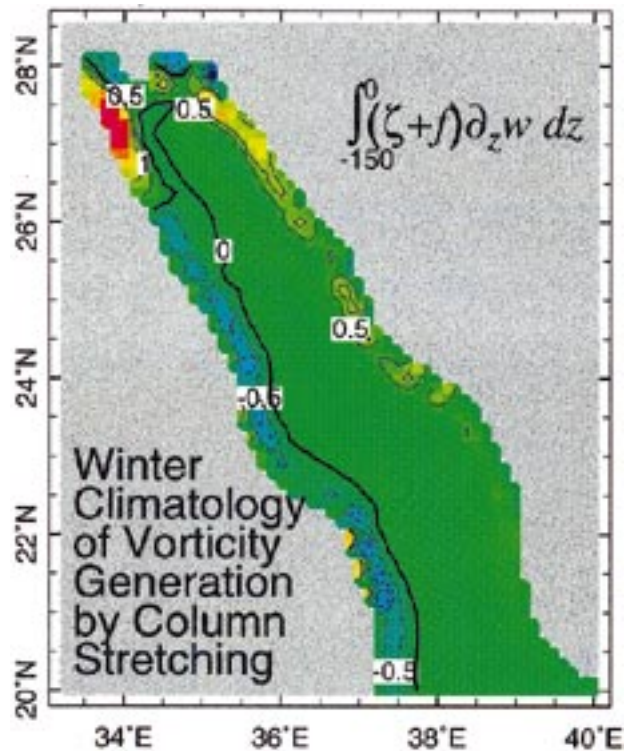


FIG. 12. Model climatological generation of relative vorticity by column stretching,  $10^{-11} \text{ s}^{-2}$ . Outside of the domain shown this term is negligible. Some of the contours are suppressed for clarity, but the color variation is maintained.

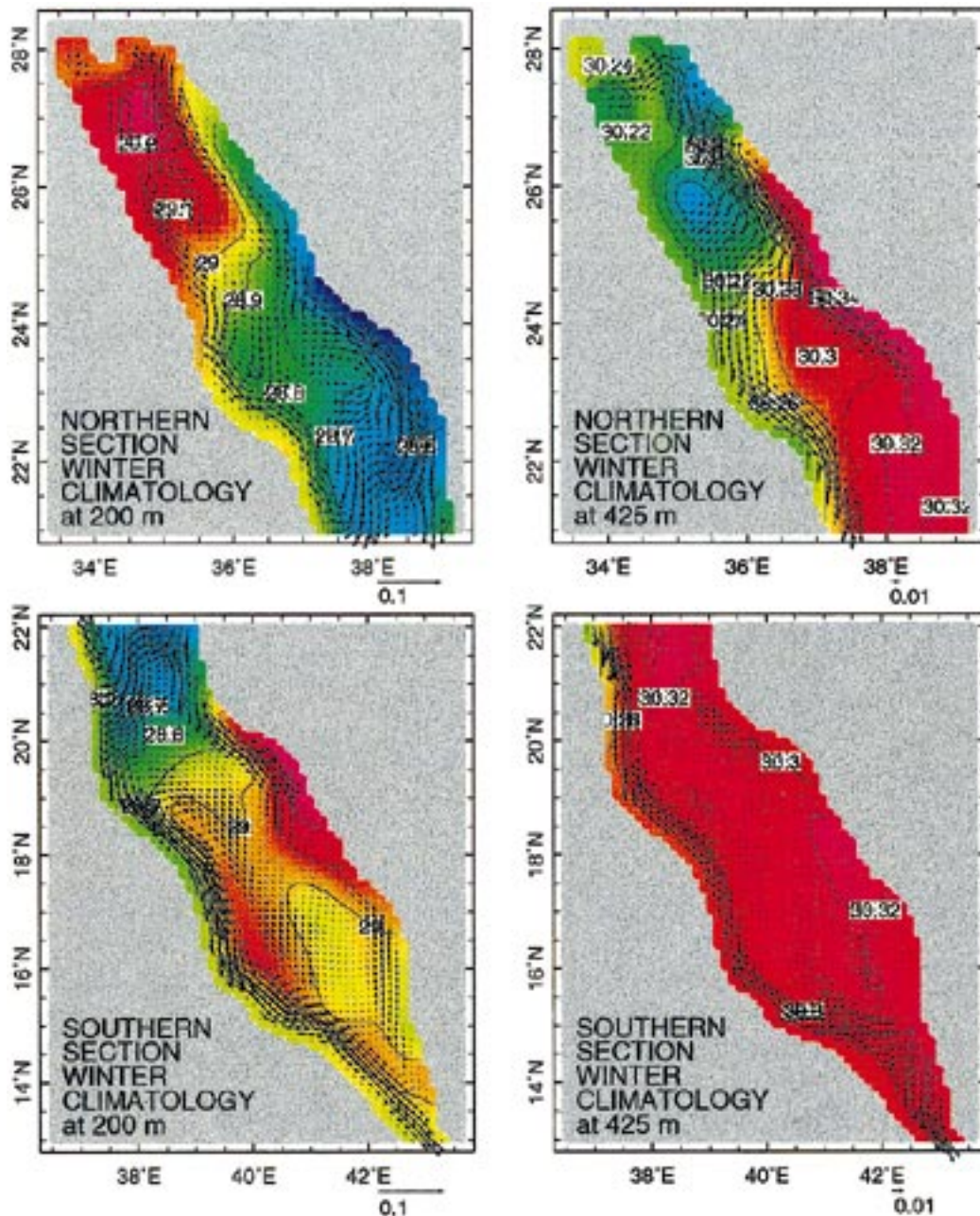


FIG. 13. Model winter climatological density ( $\sigma$ ,  $\text{kg m}^{-3}$ , colors, and contours) and flow at 200 m (left panels) and 425 m (right panels). See Fig. 1 for more details.

The situation is sharply reversed at the Red Sea's northwest corner, near the Gulf of Suez mouth, where the strongest downwelling takes place. Unlike in the interior northern Red Sea, near the northern boundary the wind dominates over the opposing pressure gradient.

The eastern boundary current flows southward along the northern boundary, collides with the western boundary, and flows southward along the western wall past the northwest corner for an additional  $\sim 100$  km. Along the western wall the basin-scale pressure gradient to the

north opposes and slows the southward flow, resulting in surface convergence. The convergence further increases the downwelling and the positive vorticity generation until 26°N, where the current terminates. Continuity at the termination point is satisfied by cyclonic turning into the interior and by downwelling. The downwelling is centered at 27.6°N at the surface and tilts southward with depth.

The surface salinity near the termination point is 40.9 psu, the highest in the Red Sea. This reflects the longest

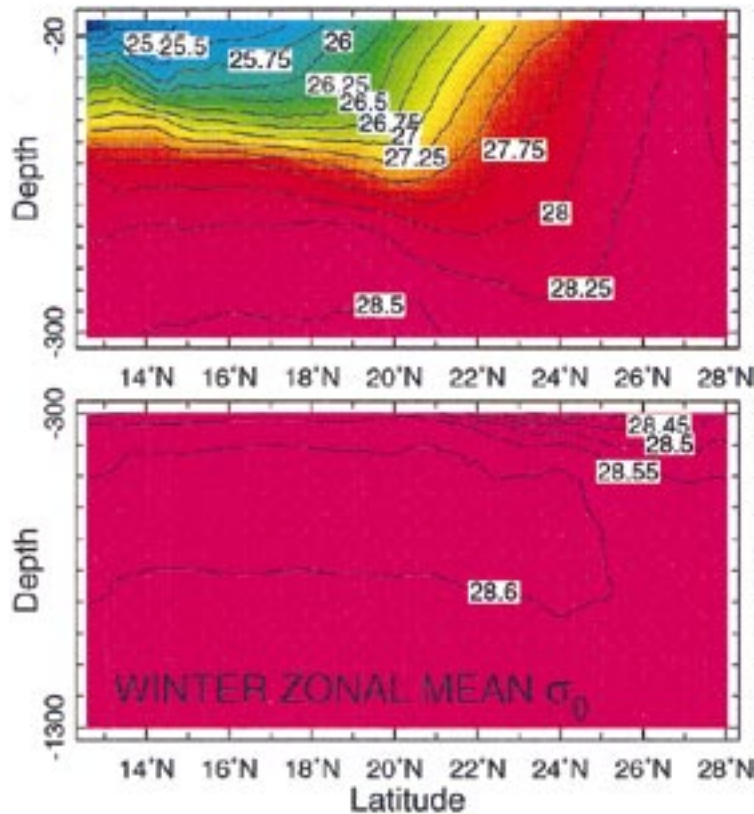


FIG. 14. Winter climatological zonal mean  $\sigma_0$  fields for the upper 1300 m,  $\text{kg m}^{-3}$ . The color scale is uniform, but the contouring interval is 0.25 in the upper panel and 0.05 in the lower.

exposure to the atmosphere. While the temperature at that point is also relatively low, the lowest temperatures are found at the center of the extreme north cyclonic gyre, where the SST is  $22.9^\circ\text{C}$ . The center of the cyclonic gyre is also the site of the highest surface density,  $\sigma = 28.3 \text{ kg m}^{-3}$ . Density cross sections in this region reveal an  $\sim 350 \text{ m}$  pycnocline doming at the center of the gyre, with which the flow is in quasigeostrophic balance. A strong observational support for such a structure is provided by Maillard (1971). Her Fig. 8 shows a  $\sigma_t$  cross section at  $27^\circ\text{N}$  in which  $\sim 200 \text{ m}$  isopycnal doming is very prominent. The observed values are lower than the computed ones, the densest being  $27.8 \text{ kg m}^{-3}$ . Since her data represent a single point in time, the difference need not be model error. This temperature structure is consistent with AVHRR brightness temperature images such as Eshel's (1996) Fig. 1.5. The satellite images, like the station data, are snapshots and are thus much more variable than the model climatologies discussed here. In spite of this difference, consistent with the model results the satellite images almost invariably show the lowest temperatures near  $26^\circ\text{--}27^\circ\text{N}$ , either at the center of the northern basin (i.e., at the center of the computed gyre) or along the western boundary. The eastern side is almost always warmer

than the west. Throughout the northern basin, the model and AVHRR also agree closely on the temperature values, as the brightness temperatures are typically between  $22.6^\circ$  and  $23.5^\circ\text{C}$ . Perhaps unexpectedly, the center of the convective activity is not at the center of the gyre, but rather along the western wall, coinciding with the site of greatest downwelling. We will return to this point later.

**4. Winter subsurface conditions**

Figure 13 shows the winter density and flow fields at 200 and 425 m. Above 200 m the circulation does not differ markedly from the upper-layer circulation presented above.

Below the surface the numerical results are not readily comparable with ECB's since the fine lateral and vertical resolutions enable the flow to vary so differently from the box model. For example, in ECB the surface layer was 40 m deep and the layer below extended to 100 m. Conversely, the numerical results do not vary considerably over these depths, especially in the northern section (where the boundary current depths are at least 200 m). In the box model, assumptions about space variability are imposed by specifying the geometry, deter-

TABLE 2. Comparison between the width- and vertical-mean transport in the winter numerical results and ECB at 40–400 m (in Sv).

Latitude	ECB	Numerical model
13.5°N	-0.39	-0.30
18.2°N	-0.38	-0.08
27.0°N	-0.22	-0.10

mining the solution to a large degree. In the numerical model, the flow may vary as it chooses. Between 40 and 400 m the width-mean flow is toward the south, as in ECB. The magnitudes differ, as Table 2 shows. The significant inconsistencies at 18.2° and 27°N may be related to concentration of the flow in boundary currents, as in the upper-layer case. Since they are narrow and undersampled, their hydrography is largely absent from ECB's dataset.

A basic test of the simulation is the model's ability to reproduce the observed hydrography; in the Red Sea the density field is the key dynamical element. Figure 14 shows the winter zonal-mean potential density field. Comparison with similar sections calculated from observed hydrography (e.g., Maillard and Soliman 1986, Fig. 6; Quadfasel and Baudner 1993, Fig. 2C) shows that the model and observed winter hydrographs are very similar.

We now continue to follow the downwelling motion at the collision point of the eastern and western bound-

ary currents. To complement the map view of the flow (e.g., Fig. 1), we use cross sections along the western boundary, shown in Fig. 15. We show below that the pressure gradient at 1300 m is very small compared to shallower depths. Consequently, we use  $\int_{-1300}^{-d} \rho dz$ , dynamic height at depth  $d$  relative to 1300 m, as a pressure proxy.

The first mechanism that removes mass from the collision site is a northeastward cross-channel flow along the northern boundary, which is apparent in the 425-m panel of Fig. 13. The  $w$  section (Fig. 15 upper right panel) shows that this flow is fed by a strong vertical convergence at 27.1°N and ~550 m. Figure 16 shows the pressure distribution that balances this flow. After crossing the channel, most of this mass forms a southeastward flowing eastern boundary current, while some upwells to 350–400 m along the eastern boundary. Thus, the flow along the north and northeast boundaries at 550 m is almost the exact opposite of the surface one.

The remainder of the eastern boundary current water continues to downwell along the western wall. As mentioned above, the downwelling center tilts to the south with depth, reaching 25.9°N at 1360 m, the deepest model interface. The  $v'$  section (lower right panel of Fig. 15) shows that at the collision point the western boundary current rides over the denser southward flow of eastern boundary current origin. Figure 17 shows that

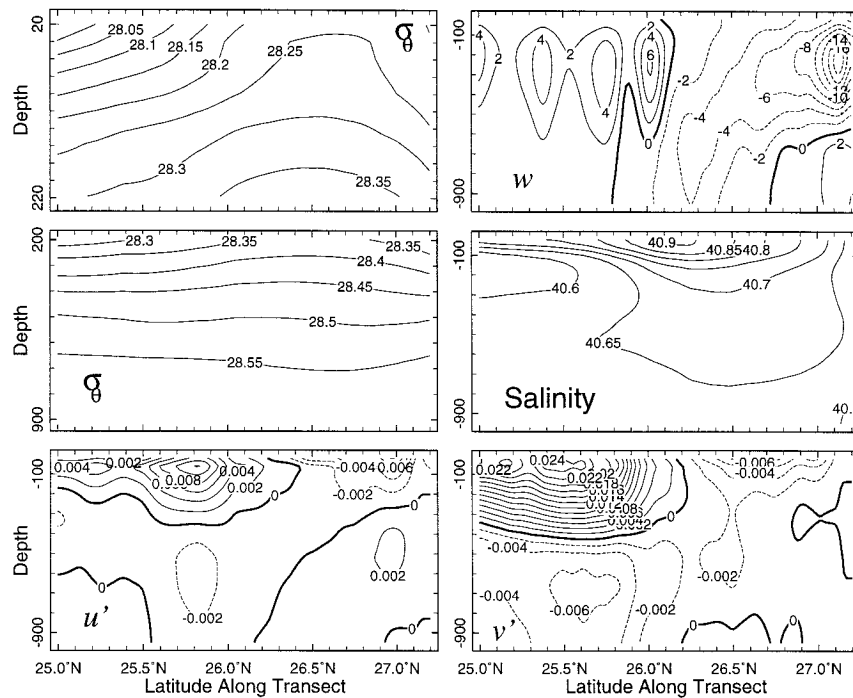


FIG. 15. Sections along the northern western boundary. The properties shown are (left column first, top to bottom):  $\sigma_\theta$  ( $\text{kg m}^{-3}$ , upper 200 m, and 200 to 900 m);  $u'$ , the velocity normal to the transect, positive to the northeast (toward the reader) ( $\text{m s}^{-1}$ ); upwelling ( $\text{m day}^{-1}$ ); salinity (psu); and  $v'$ , the northwestward velocity along the transect ( $\text{m s}^{-1}$ ).

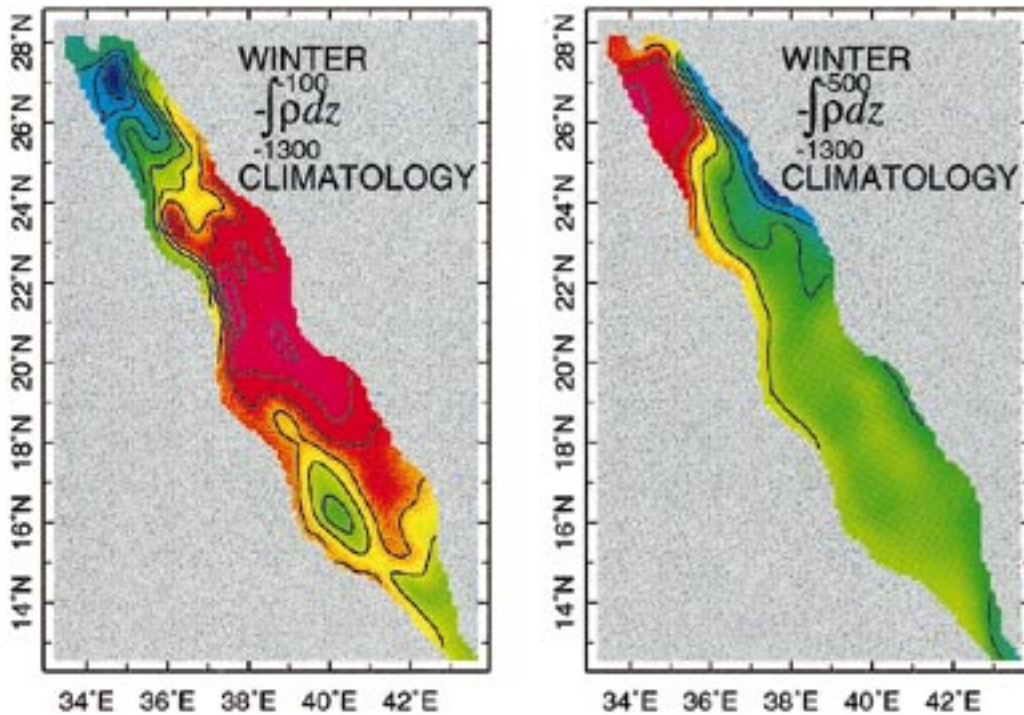


FIG. 16. Winter climatological  $\int_{-1300}^{-d} \rho dz$ , approximately the pressure field at  $d$ ;  $\text{kg m}^{-2}$ . Left panel:  $d = 100$  m; right panel:  $d = 500$  m. Since it is a relative measure, we do not show values; high pressure at  $d$  is shown by the “warm” colors, while green and blue correspond to low pressures.

throughout the entire vertical extent of the western boundary current, it is lighter than the eastern current. Thus, the western boundary current is forced to leave the coast. This motion is most pronounced at  $\sim 25.9^\circ\text{N}$  and 100 m, as the  $u'$  panel of Fig. 15 shows, but is also clear at 200 m (Fig. 13). The 100-m panel of Fig. 16 shows that this flow coincides with, and is driven by, a local maximum in the northward pressure gradient. Be-

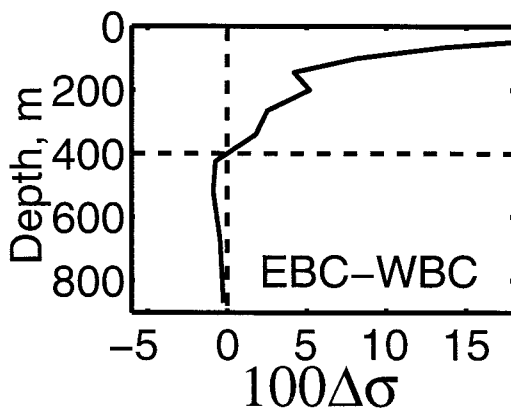
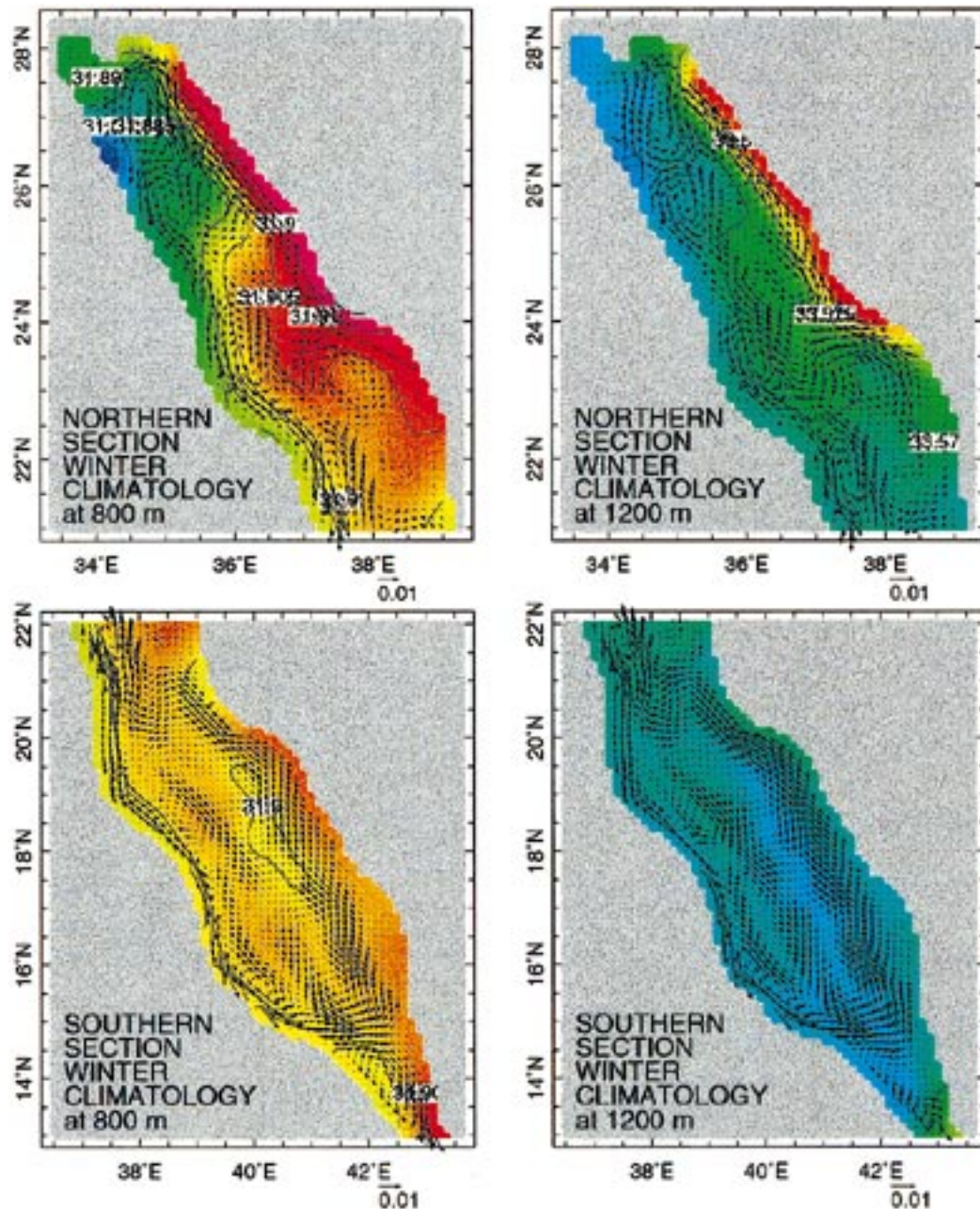


FIG. 17. In situ density difference between the eastern and the western boundary currents as a function of depth, m;  $\sigma_{\text{EBC}} - \sigma_{\text{WBC}}$  in  $\text{kg m}^{-3}$ . The vertical dashed line is the zero difference line, and the horizontal one shows the vertical extent of the western boundary current.

cause the eastern boundary current is denser, its remainder (after shedding the cross-channel eastward flow at  $27.1^\circ\text{N}$ ) subducts under the western boundary current. The  $\sigma_\theta$  sections (the two upper-left panels in Fig. 15) show this path in the outcropped isopycnals south of the collision point.

The forced sinking and the isopycnal outcropping affect each other; the outcropping steers the subduction, but the subduction also maintains the outcropping. Outcropping-maintenance by the sinking motions can best be inferred from Fig. 15, where the salinity “bowl” and the density dome coincide at  $26.5^\circ\text{N}$ . We can estimate the haline density effect of the vertical motions. With a vertical-mean  $\theta = 22.8^\circ\text{C}$  and  $S_{\text{surface}} - S_{\text{middepth}} \approx 0.22$  psu, the sinking-related  $\delta\sigma_\theta \approx 0.17 \text{ kg m}^{-3}$ . The actual  $\delta\sigma_\theta \approx 0.3 \text{ kg m}^{-3}$  due to the stable temperature profile; the surface water must cool before sinking. This is the combined role of the surface fluxes and convection, as discussed in section 5. Thus, the subduction does not proceed passively along outcropped isopycnals, nor is outcropping purely thermodynamic; rather, the outcropping and the subduction are dynamically linked.

The subduction and its accompanying mass rearrangement penetrate to middepth. While the densest surface water is found at the extreme northwest near the collision site, at 300 m only a small patch of anomalously dense water remains in the northern basin. By 425 m the surface picture is already fully reversed (Fig.



crosses the channel to the western wall. The flow proceeds along the western wall all the way south, exiting the Red Sea through the strait. (Any flow across the strait at that depth is spurious and is due to the absence of topography from the model. However, it is negligible compared to upper-layer flow through the strait, as discussed in section 3.) This structure does not change markedly with depth (Fig. 18), with two exceptions. The first is the flow through the strait. It diminishes with depth, with a larger fraction of it recirculating to the north away from the western boundary. Combined, the deep southward western boundary current and the northward recirculation in the southern basin interior form a nearly closed cyclonic abyssal circulation cell. This cell is strikingly similar to the barotropic flow shown in Fig. 5. Evidently, at these depths the barotropic flow dominates. (This justifies using 1300 m as the level of no motion.) The flow in the southern basin at depth is probably one of the least realistic elements of our simulation. Eshel's (1996) Fig. 4.21 shows the Red Sea bathymetry. While in the northern basin, on which we focus, the deviation of the real bathymetry from that of the model is rather small, in the southern basin it is by no means negligible. The wide and gradual shelves restrict depths greater than 500 m to a very narrow strip, which is clearly at odds with our simulation.

The second marked difference between the middepth and abyssal circulations is the eastern boundary current in the northern basin. The middepth southward flowing eastern boundary current weakens with depth, until at 1200 m it is fully reversed, flowing to the north. The reversal is clearly related to the high-density anomaly along the northeastern boundary, which extends from 600 m to the bottom. This anomaly is the "reduced gravity" compensation for the upper-layer low density anomaly. In section 3, we attributed the upper-layer anomaly to convergence of the eastward cross-channel flow near the eastern wall. The deep high-density anomaly source is the sinking water from the collision site that fills the northwest basin from the western wall. In comparison to the water of western boundary origin, the eastern boundary middepth and deep waters are denser. In the deep northern basin from 600 m to the bottom there are two weak eddies: an anticyclonic one, centered around  $\sim 27^\circ\text{N}$ , and a cyclonic one, centered around  $\sim 25.5^\circ\text{N}$ . They are both related to mass distribution that compensates for the overlying density anomalies. The northern one compensates for the upper-layer cyclonic gyre, while the southern one compensates for the middepth low-density anomaly. In both, the velocities are sufficiently small compared to upper-layer motions to conform with the 1300 m "level of no motion."

## 5. Winter results: Discussion

We have outlined a dynamical framework for the Red Sea in the winter. The collision of the eastern and western northward flowing boundary currents near the north-

west corner of the Red Sea triggers a number of processes, such as boundary current termination and cross-channel flow. The most intriguing of these is the subduction of the eastern boundary current under the western one. Cember (1988) was the first to suggest that such a process takes place in the northern Red Sea. The theorized subduction enabled Cember to elegantly resolve what seemed a major discrepancy between the observed vertical structure of temperature and salinity and that of tracers such as  $^3\text{He}$  and  $^{14}\text{C}$ . This issue is discussed exhaustively by Cember (1988) and ECB; its essence is that hydrographic properties vary sharply in the upper  $\sim 200$  m and hardly at all below that, while tracers vary smoothly and gradually in the upper  $\sim 600$  m. The former suggests upwelling dominance and little mixing, while the latter is consistent with active mixing and downwelling. The resolution is provided by the conjectured subductive mode, with hydrographic characteristics of deep water, along with tracer signatures intermediate between the surface and middepth values. Later, ECB supported this interpretation as well as its estimated magnitude. However, both of these papers analyzed the data two-dimensionally, offering no dynamical mechanism beyond the generic thermodynamic surface forcing. It is particularly important that our numerical results contain this process, allowing us to analyze its dynamics. While the model's flat bottom is a major shortcoming, at the collision site, the 500-m isobath almost coincides with the western boundary [Eshel's (1996) Fig. 4.21]. This might suggest that in the vicinity of the collision point the simulation will not be dramatically altered by the addition of realistic topography.

The model collision-related sinking differs from Cember's proposed mechanism in two related ways. The first is the depths it renews. Cember's isopycnal mode resolves the above tracer-hydrography discrepancy only if it ventilates the upper deep water, 150–300 m. In the model, the sinking motion continues to  $>1$  km, but is most pronounced in the depth range 400–600 m. This can be related to the absence of bathymetry from the current model formulation, as the following heuristic argument suggests. Let  $V$  denote the downwelling volume, which is compensated for by upwelling  $w(x, y, z)$  over an area  $A(z)$ . Mass continuity requires  $V = \int \int w dx dy = A(z)\bar{w}(z)$  (where the overbar denotes spatial averaging), or  $\bar{w}(z) = A(z)^{-1}V$ . Next we take depth derivatives

$$\frac{d\bar{w}}{dz} = \frac{1}{A(z)} \frac{dV}{dz} - \frac{V}{A(z)^2} \frac{dA}{dz}.$$

From Fig. 15, in the upper 900 m  $dV/dz \approx 0$ , so

$$\frac{d\bar{w}}{dz} \approx -\frac{V}{A(z)^2} \frac{dA}{dz}.$$

(That  $A^{-1}dV/dz \ll A^{-2}VdA/dz$  can also be shown by simple scale analysis, which we do not repeat here.)

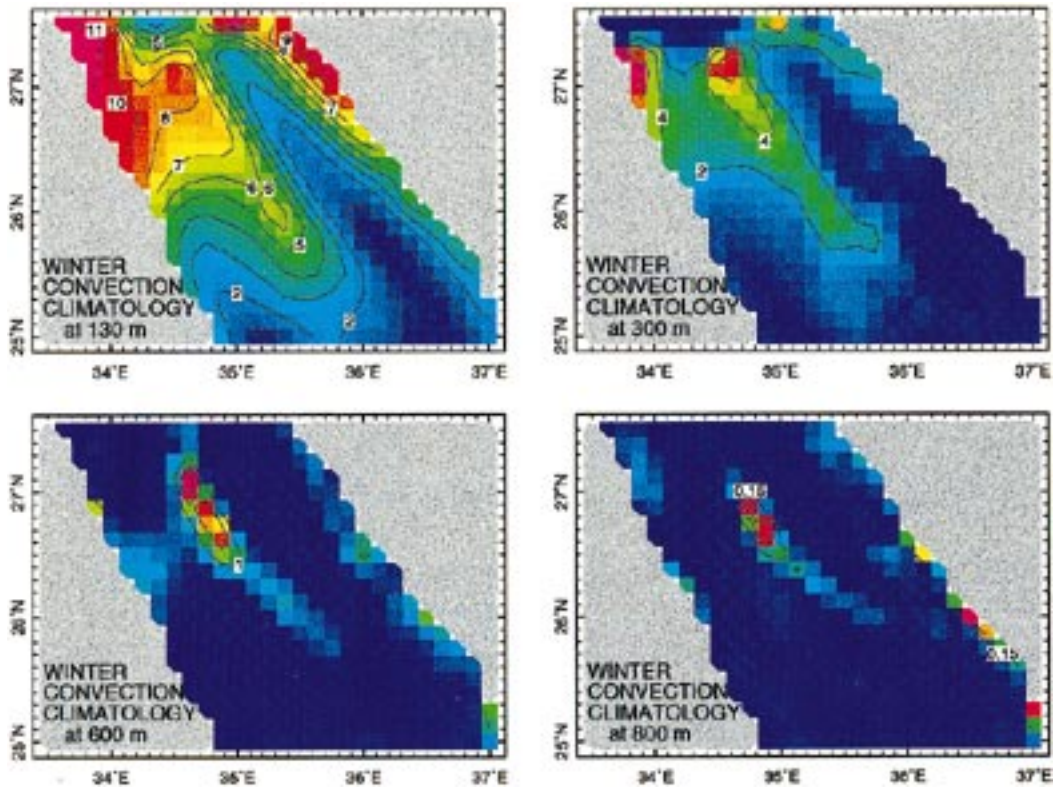


FIG. 19. Winter climatological convection. The plotted variable is incremented every time convection takes place by the difference between the potential energy of the two layers in question before and after the convection; see text for definition. Little convection occurs outside the area shown.

Since  $dA/dz > 0$  [see Eshel's (1996) Fig. 4.21 for the detailed bathymetry],  $d\bar{w}/dz < 0$  and  $w$  increases with depth. Below a certain depth the increased upwelling becomes inconsistent with the rest of the dynamics and can also oppose the downwelling directly. Thus, we believe the depth of penetration of collision-related dynamics is probably exaggerated.

The second inconsistency between our results and Cember's is related to the details of the sinking. In Cember's interpretation, the isopycnal mode (his shorthand for the process) subducts along the outcropped isopycnals. Typically this refers to convective mixing along tilted isopycnals. In the model, on the other hand, the mass flux is accomplished by climatological seasonal-mean vertical velocity. The question then arises as to whether the model downwelling and Cember's isopycnal mode are the same process.

Cember (1988) defined Red Sea Deep Water below the sill depth by  $T < 22^\circ\text{C}$ ,  $S > 40.4$  psu. With such  $T$  and  $S$  at 400 m, the deep water's  $\theta \leq 21.9^\circ\text{C}$  and its  $\sigma_\theta \geq 28.36$  kg m $^{-3}$ . The potential density sections (Figs. 14 and 15) show that, even at the peak of the model density dome, this isopycnal does not surface. To acquire deep-water density, the water must lose buoyancy at the downwelling area. This clearly happens at the surface, but below the surface  $d\rho/dt \approx$  mixing. Com-

municating the surface fluxes to the subsurface water as it descends is the role of shallow convection, which we have so far neglected.

Figure 19 shows a quantitative measure of convective activity. The measure is incremented every time convection is performed by  $\delta c = [\rho_{k+1}h_{k+1}/2 + \rho_k(h_{k+1} + h_k/2)]^i - [\rho_{k+1}h_{k+1}/2 + \rho_k(h_{k+1} + h_k/2)]^{i+1}$ . Here  $\rho$  and  $h$  are density and thickness,  $k$  and  $i$  are the layer and convective time indices, and the spatial index is suppressed for clarity. The measure is sensitive to the magnitude and vertical scale of the static instability. The spatial structure is unexpected. Convection is usually associated with the eroded stratification in upwelling areas, but here the convection coincides with the most intense downwelling. As the water sinks and is disconnected from the surface fluxes, it approximately conserves its potential density. However, the surface water above loses buoyancy throughout the winter, and static instability follows. Thus, the quasi-steady-state winter picture includes the continuous generation of static instability by the combination of sinking motions and intense surface buoyancy loss and its removal by convection.

Figure 20 is a map of the depth  $h$  above which the total buoyancy content, defined by  $-g\rho_0^{-1} \int_{-h}^0 [\rho(z) - \rho_h] dz$ , is equal to the seasonal buoyancy loss  $\int_{t_1}^{t_2} B_0 dt$ .

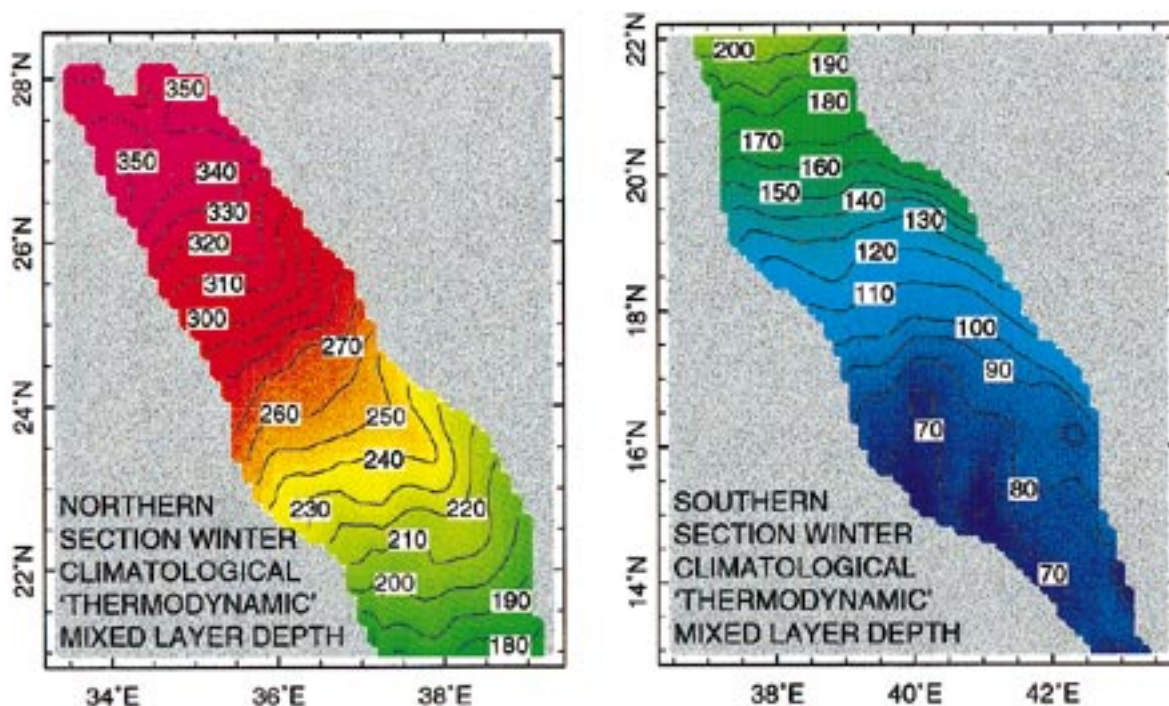


FIG. 20. Winter climatological depth of penetration of thermodynamic stirring,  $h$ , defined by  $-g\rho_0^{-1} \int_{-h}^0 [\rho(z) - \rho_h] dz = \int_{t_1}^{t_2} B_0 dt$ . See text for symbols and other details.

Here  $B_0$  is the surface buoyancy flux per unit time (Fig. 9) and  $t_1$  and  $t_2$  are the season's beginning and end ( $t_2 - t_1 = 180$  days). Figure 20 shows that the thermodynamics adds to the dynamics in favoring convective communication between the sinking motions and the surface fluxes. We conclude that the collision and sinking motions in our results are the dynamical elements of Cember's isopycnal mode. To estimate the flux associated with this mode in the model, we assume the convection does not transfer any mass, but only maintains the stability. Thus mass is transferred only by the vertical velocity. With a sinking area roughly 25 km wide by 145 km long and a mean vertical velocity of 3 m day<sup>-1</sup>, the annual continuous flux into the upper deep-water mass is 0.12 Sv. Remarkably, based on entirely different considerations, Cember (1988) estimated the isopycnal mode flux as 0.11 Sv.

Below the downwelled water the convection weakens by two orders of magnitude, and its maximum shifts to the center of the cyclonic gyre where the stratification is weakest. There appear to be two distinct deep-water formation processes in the Red Sea. The shallow-convective, subductive mode is related to a basin-scale pressure gradient. As discussed previously, the pressure gradient results from the cumulative effect of ocean-atmosphere interactions on the surface water as it flows from the Gulf of Aden to the northern RS. In section 3 we showed that the characteristic timescale for this "aging" process is a few years. Consequently, subductive water mass formation is likely to vary on long time-

scales. On the other hand, the center of the cyclonic gyre in the northern Red Sea is very weakly stratified throughout the winter. It seems plausible that this is the site of episodic deep convection in response to short-lived intense atmospheric events.

To develop the argument, consider the significant difference in the seasonal cycles of freshwater and heat surface fluxes (Fig. 8). The freshwater flux is highly negative throughout the year. The summer loss is more than the winter's, with a >2.5 m yr<sup>-1</sup> maximum in a narrow strip along the northwestern boundary, exactly over the collision site. Conversely, the summer surface heat loss is considerably less than in winter and is actually a heat gain in the extreme north. While we showed earlier that the collision-related downwelling still requires a substantial heat loss, preconditioning of the surface water by the evaporative loss throughout the entire several year journey to the north is crucial. The final thermal buoyancy loss is climatologically available near the collision site during the winter. This is sharply contrasted with the thermal contribution to deep convection, which we speculated takes place in the center of the northern cyclonic gyre. Because in summer the ocean actually gains heat and because the climatological SSTs are not low enough to permit convection, it is tempting to conjecture that deep convection is related to episodic atmospheric events, which are suppressed in climatological forcing.

In the introduction, we stated that this work is partly motivated by the hope that our findings from the Red

Sea can serve as analogs of global-scale processes. Thus, we would like to conclude the discussion by pointing out the potential importance of our results to the study of planetary-scale wind-driven circulation. The related problems of the interactions between the subtropical and subpolar gyres and the separation of western boundary currents from the wall are still far from solved (e.g., Hsueh et al. 1996; Huang 1991; Schmitz and McCartney 1993). The vastness of the subtropical-subpolar boundary regions, and their characteristic high-frequency variability, make the planetary-scale problem a formidable one indeed. In this respect, a somewhat similar, yet much smaller and simpler, boundary current collision and separation site can offer important insights. We will pursue this issue elsewhere.

## 6. The winter planetary boundary layer

Figure 8 shows the model total surface heat flux and net evaporation. These, as well as the former's partitioning between the various terms, are calculated rather than specified. They are also foremost in determining the surface ocean conditions, which are a key element of our story. Hence, the planetary boundary layer warrants a careful analysis, which is the purpose of this section.

The Red Sea presents the boundary layer model with a unique challenge. One of the model's underlying assumptions is that the boundary layer is well mixed. Typically this is the case over the ocean since the lower atmosphere's source of both heat and moisture is the underlying ocean. The situation over the Red Sea is at times different because of the unusually hot and dry surrounding land masses (Fig. 22). To account for these somewhat unusual circumstances, we have modified the PBL model as follows. First, we have reduced the assumed PBL thickness from 600 to 300 m. Since the model has a fixed thickness, this represents a time average of a thick, unstable boundary layer and a thin, stable one. Second, we have set the entrainment at the top of the PBL to zero under stable conditions. This accounts for the fact that under stable conditions the PBL does not have a buoyancy source at its bottom. Finally, we have replaced  $C_0$ , the fixed transfer coefficient that governs evaporation and sensible heat flux in Seager et al.'s (1995) PBL model formulation with Smith's (1988) stability-dependent values. Judging a posteriori from the model success in reproducing observed surface fields, these changes proved sufficient.

### a. The solar flux

The first-order winter surface heat balance is between latent heat loss and incident solar radiation. Since the latter is an input to the model, it is worthwhile checking it against other datasets. The ERBE winter data are, on average,  $25.1 \text{ W m}^{-2}$  lower than da Silva et al.'s (1994) and  $2.5 \text{ W m}^{-2}$  higher than Oberhuber's (1988). While Oberhuber's data are absorbed solar radiation, da Silva

et al.'s are the incoming shortwave radiation, that is, not corrected for albedo. When they are multiplied by 0.91 (assuming a mean albedo of 9%), the mean difference reduces to  $6.3 \text{ W m}^{-2}$ . We conclude that the ERBE data over the Red Sea are adequate.

### b. The latent heat flux

The latent heat flux is given by  $\rho_a L C_0 \|W\| (q_s - q_a)$ . The symbols represent respectively air density, latent heat of vaporization, stability-dependent transfer coefficient, wind speed, and specific humidities at saturation and at the actual air temperature. Thus, the latent heat flux field (Fig. 21) reflects gradients of stability (Fig. 22), scalar wind speed ( $\sim 8 \text{ m s}^{-1}$  at  $27.5^\circ\text{N}$ ,  $< 5 \text{ m s}^{-1}$  at  $16^\circ\text{N}$ , and  $> 9 \text{ m s}^{-1}$  at  $13^\circ\text{N}$ ), and SST (of which  $q_s$  is a function; Fig. 3). Also,  $q_a$  depends on evaporation and advection of the specified land boundary values by offshore specified winds. Figure 23 shows the boundary layer variables relevant to the latent heat flux. From it, and from the above values, we can identify the important processes. The stability-dependence of  $C_0$  is weak and does not contribute much to the variability. Because the wind speed at  $27.5^\circ\text{N}$  is 1.6 times stronger than at  $16^\circ\text{N}$  (8/5), wind speed variability accounts for a 60% latent heat loss increase from  $16^\circ\text{N}$  to the extreme north; the actual increase is 85% (from a minimum of  $116 \text{ W m}^{-2}$  near  $16^\circ\text{N}$  to a maximum of  $215 \text{ W m}^{-2}$  in the north). South of  $16^\circ\text{N}$  the wind nearly doubles (to  $> 9 \text{ m s}^{-1}$ ), with a latent heat loss increase of only  $\sim 25\%$  (to  $146 \text{ W m}^{-2}$ ). In absolute terms, with a mean  $q_s - q_a \approx 0.008$ , the wind speed effect is  $24 \text{ W m}^{-2}$  per  $1 \text{ m s}^{-1}$ . Thus, while wind speed variability is important, it is not the only player.

The rest of the variability is related to the humidity patterns. Unlike the open ocean, where evaporation can shut itself off by increasing  $q_a$  to saturation ( $q_a \approx q_s$ ), the northern Red Sea is constantly supplied with continental dry air from the upstream Sinai peninsula. The effect is shown in the  $q_a$  panel of Fig. 23, where the lowest values are at the extreme north. Compared to other oceanic boundary layers, the specific humidity values themselves are actually quite high due to the relatively high temperatures (a fact that creates large  $\theta_s - \theta$  values). With a mean wind speed of  $7 \text{ m s}^{-1}$ , the  $3 \times 10^{-3}$  north-south difference in  $q_s - q_a$  corresponds to latent heat loss difference of  $75 \text{ W m}^{-2}$ .

In conclusion, the latent heat loss minimum at  $16^\circ\text{N}$  near the western boundary is in response to both reduced wind speed and a moisture maximum due to surface moisture convergence. The associated heat convergence is negative because the temperatures are lower upstream from the convergence zone to the north and south. Consequently, the relative humidity also attains a maximum at the convergence zone (i.e.,  $q_a \rightarrow q_s$ ), which inhibits evaporation. Between the convergence zone and the extreme north the latent heat loss increases considerably. This is due to enhanced wind speeds and reduced mois-

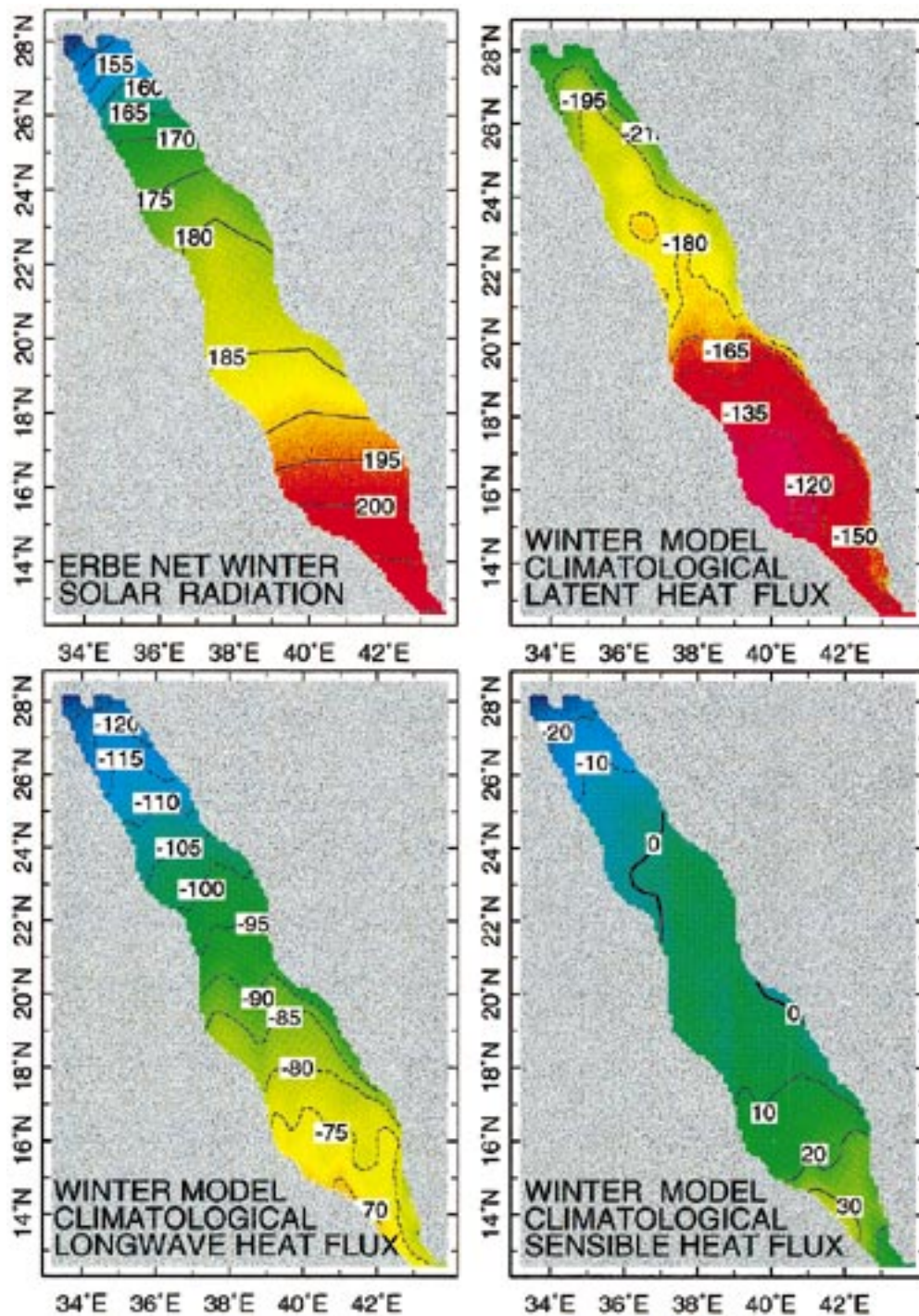


FIG. 21. Winter climatological calculated surface fluxes ( $W m^{-2}$ ).

ture. From the convergence zone to the strait the latent heat loss also increases. The increase rate is slower than to the north, in spite of the rapid intensification of the wind speed to a domain-maximum of roughly  $10 m s^{-1}$ . This is due to the advection of high-humidity air of tropical Indian Ocean origin.

*c. The longwave radiative cooling*

The next significant term in the surface heat budget is the longwave radiative cooling. Following Seager and Blumenthal (1994), the longwave heat flux is given by  $\epsilon\sigma\theta_a^4(f_1 - f_2e^{1/2})(1 - f_3C^2) + 4\epsilon\sigma\theta_a^3(T_s - \theta_a)$ . Here  $\epsilon$  is

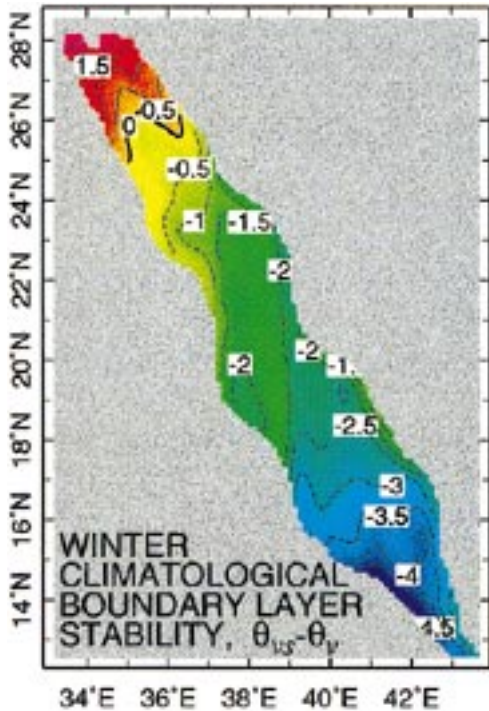


FIG. 22. Stability of the winter boundary layer,  $\theta_w - \theta_a$ . Here  $\theta_w$  and  $\theta_a$  are the air virtual potential temperature at the SST (i.e., at saturation) and at the actual air temperature. Negative values correspond to a stable boundary layer.

sea water emissivity (0.97),  $\sigma$  is the Stefan–Boltzmann constant,  $f_1 = 0.435$ ,  $f_2 = 0.048$ ,  $e$  is the surface vapor pressure ( $p_s q_a 0.622^{-1}$ , where  $p_s$  is the surface pressure, taken as 1000 mb),  $f_3 = 0.54$ ,  $C$  is the cloud cover fraction (da Silva et al. 1994), and  $T_s$  is the SST. See Seager and Blumenthal (1994) for a detailed discussion. In addition to slightly different coefficient values, we have modified the leading term from  $\propto T_s^4$  to  $\propto \theta_a^4$ . This reflects the assumption that the effective (net) radiation is not from the actual ocean surface, but rather from the boundary layer. (The ability to make this assumption is a major advantage of the PBL model. While in most of the open ocean  $T_s \approx \theta_a$ , in the Red Sea this cannot be generally assumed, and often  $T_s \ll \theta_a$ , such that the actual radiative cooling of the coupled boundary layer–sea surface system is much more adequately represented by  $\theta_a$ .) Figure 21 shows that in winter the radiative cooling increases monotonically from  $70 \text{ W m}^{-2}$  near the strait to  $\sim 125 \text{ W m}^{-2}$  at the extreme north. The fractional cloudiness variability, 0.26 to 0.36, accounts for a small fraction of the radiative cooling variability. For mean conditions, the full amplitude of the cloudiness variability translates to a longwave cooling variability of less than  $10 \text{ W m}^{-2}$ . The remaining sources of radiative cooling variability are the fields of  $\theta_a$  (Fig. 23),  $e^{1/2}$  (which can be inferred from the  $q_a$  field of Fig. 23) and  $\text{SST} - \theta_a$  (varying gradually from  $-2.2 \text{ K}$  near

the strait to  $3.25 \text{ K}$  at the extreme north). With these temperature differences and  $\bar{\theta}_a \approx 300 \text{ K}$ , the radiative cooling additive term varies from  $-13.3 \text{ W m}^{-2}$  near the strait to  $19.3 \text{ W m}^{-2}$  at the extreme north, or about  $30 \text{ W m}^{-2}$ .

Next we examine the  $\theta_a$  contribution to radiative cooling variability. With  $\bar{q}_a = 1 \text{ g kg}^{-1}$ ,  $\bar{C} = 0.25$ , and  $\theta_a$  varying from  $294 \text{ K}$  at the extreme north to  $303 \text{ K}$  near the strait, the leading term of the longwave flux varies from  $149$  to  $169 \text{ W m}^{-2}$ . This contribution is opposite to the  $\text{SST} - \theta_a$  variability, since here the cooling decreases to the north.

The last source of radiative cooling variability is  $q_a$ . From Fig. 23 and the expression for the longwave flux it is clear that moisture works against the  $\theta_a$  contribution to radiative cooling since both air temperature and moisture are lowest in the north, but their effects have opposite signs. With assumed  $\theta_a = 298 \text{ K}$  and  $C = 0.3$ , the  $q_a$  (which varies from  $0.7 \text{ g kg}^{-1}$  at the extreme north to  $1.4 \text{ g kg}^{-1}$  near the strait) forces a radiative cooling decrease from  $159 \text{ W m}^{-2}$  in the north to  $150 \text{ W m}^{-2}$  near the strait. Thus, the variability of both  $q_a$  and  $\text{SST} - \theta_a$  cause larger radiative losses in the north, and their combined effect is somewhat attenuated by the  $\theta_a$  opposing contribution. Since the latter is small, the resultant heat loss is maximized at the extreme north.

#### d. The sensible heat flux

The sensible heat flux is given in Fig. 21. While it is rather small, its variability cannot be ignored. Given by  $\rho_a c_p C_0 |W| (\text{SST} - \theta_a)$  (where  $c_p$  is the specific heat of water), the sensible heat flux reflects the variabilities of wind speed and air–sea temperature difference. Since both increase to the north as discussed above, so does the sensible heat loss. From the atmospheric convergence zone ( $\sim 18^\circ\text{N}$ ) to the strait the wind intensifies again, and the ocean is colder than the air. Thus, the sensible heat flux is into the ocean.

## 7. Summer conditions

As was stated at the introduction, this paper’s prime interest is subsurface ventilation. Consequently, we focus mostly on the winter. In this section we briefly review the summer conditions, only to the extent that they shed some new light on the water mass formation processes previously described.

Figure 24 shows the summer surface conditions. Surprisingly, in spite of the different wind regimes the summer and winter climatologies are not dramatically different. This counters the commonly held view about the Red Sea seasonal circulation (e.g., Patzert 1972a,b; ECB). The meridional fluxes (Fig. 2) agree with ECB only at  $27^\circ\text{N}$  (Table 3). The discrepancies elsewhere may in part be related to the fact that the current results are a time average of a 6-month period centered around August (as described in section 2). The wind reversal, which

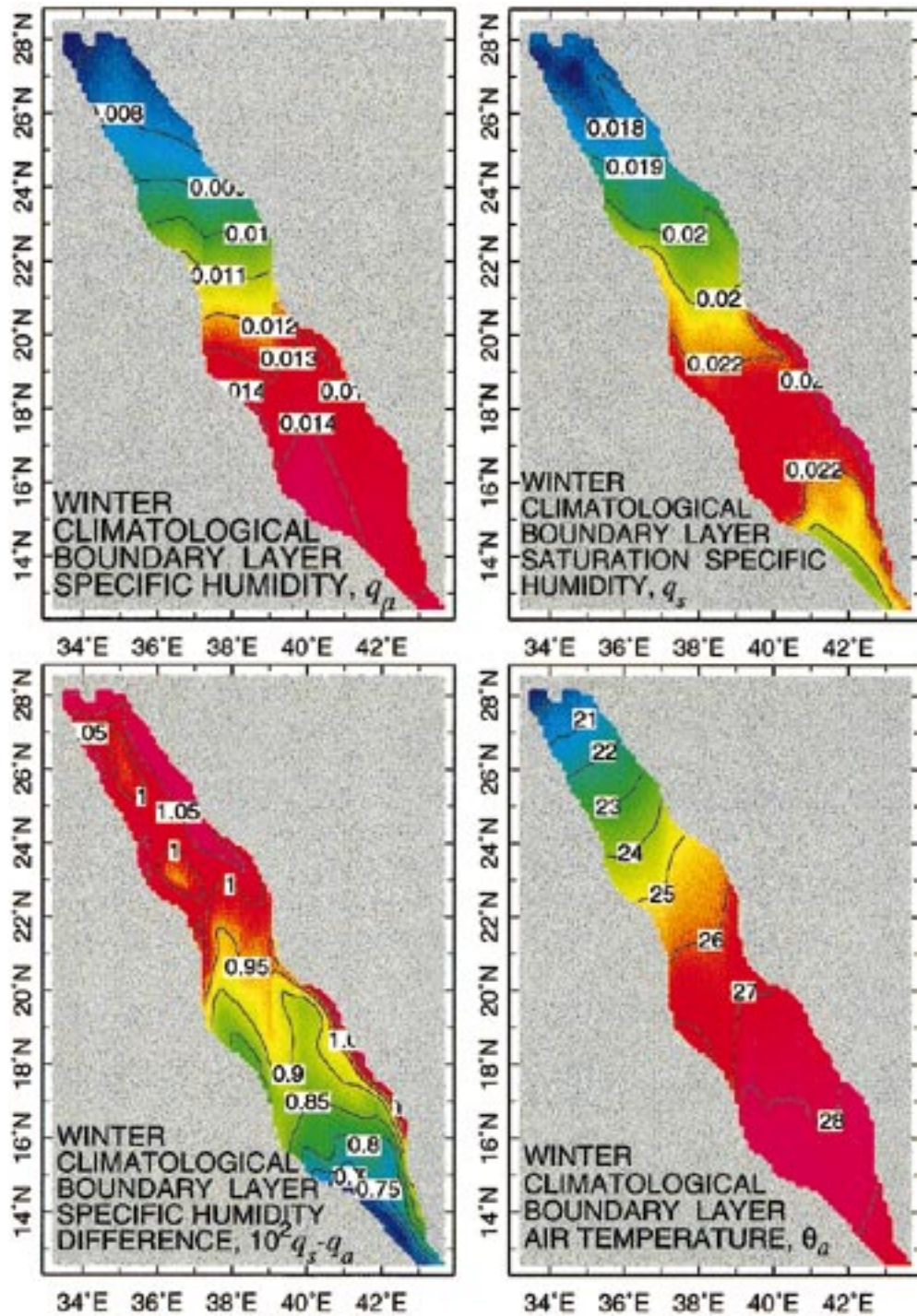


FIG. 23. Winter climatological calculated PBL parameters relevant to the latent heat flux. Specific humidity is given in kg water vapor per kg air. The  $q_s - q_a$  panel is multiplied by  $10^2$  for clarity.

drives the oceanic seasonal reversal argued by Patzert (1972a,b) and others, is short lived [see ECB and the review in Eshel (1996) for a discussion]. For example, in da Silva et al.'s (1994) data the wind in the southern basin is to the south only in the peak of summer. During

both transition seasons the wind pattern is much more similar to that in winter (i.e., to the north) than in the summer. Thus, the presented semiannual mean centered around August can reflect dominance of the transition periods over the relatively brief summer regime.

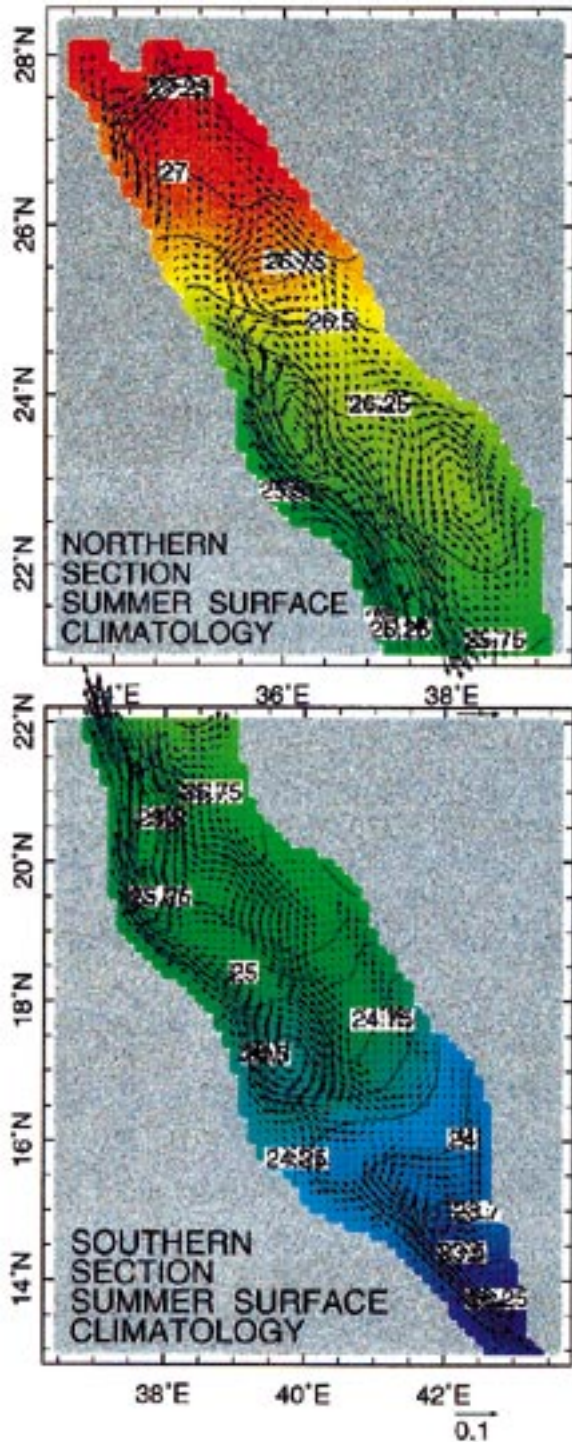


FIG. 24. Model summer climatological upper 20-m density ( $\sigma$ ,  $\text{kg m}^{-3}$ , colors, and contours) and flow. The scale vector ( $\text{m s}^{-1}$ ) and the color scheme are uniform.

TABLE 3. Comparison between the width- and vertical-mean upper-layer summer transports in the numerical results and ECB (in Sv).

Latitude	ECB	Numerical model
13.5°N	-0.17	+0.15
18.2°N	-0.14	+0.02
27.0°N	-0.07	-0.07

The surface flux seasonality (Figs. 8 and 9, discussed in section 3) ultimately drives most seasonal differences. The significantly reduced buoyancy loss permits restratification. This effect is clear in the northern basin (Figs. 25 and 26). The intense anomaly near the strait is shallow. In the southern basin the amplitude of the stratification seasonal cycle decays rapidly with depth, and by  $\sim 150$  m it is essentially zero. In contrast, at 27°N  $\sigma_{\theta}^{\text{winter}} \neq \sigma_{\theta}^{\text{summer}}$  to  $\sim 600$  m. While in most of the northern basin the eastward cross-channel flux between the western and eastern boundary currents continues (Fig. 27), there are important exceptions (e.g., the 23°N panel of Fig. 27 and Fig. 28). The westward Ekman flux is possible because of the concentration of the wind forcing over the much shallower upper layer, and because of the reduced sea-surface tilt.

The northward flowing boundary currents are narrower, and the eastern one is also considerably weaker due to reduced eastward cross-channel flow. The reduction in both cross-channel flow and the accompanying surface convergence along the eastern boundary reflect two changes. The first is the diminished summer large-scale pressure gradient discussed in section 3. The second is the recirculation to the south of a large fraction of the western boundary current's volume immediately to the east of the current. This recirculation deprives the eastward cross-channel flow of a significant portion of its source, thus weakening it. This recirculation pattern is related to the absence of the newly downwelled, relatively light, water mass of eastern boundary current origin from the northern basin in the summer. Below we return to this point after discussing the collision site

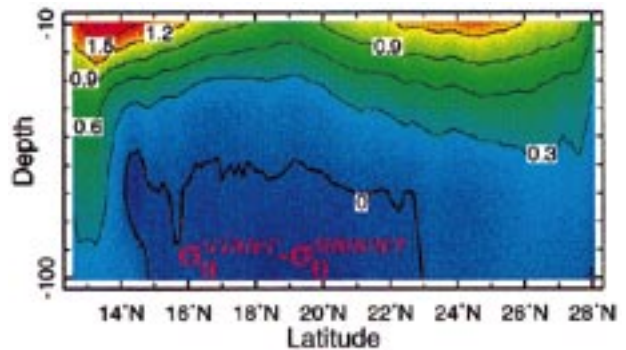


FIG. 25. Model climatological winter–summer zonal mean  $\sigma_{\theta}$  difference,  $\text{kg m}^{-3}$ . Below the shown depth, the changes are very small.

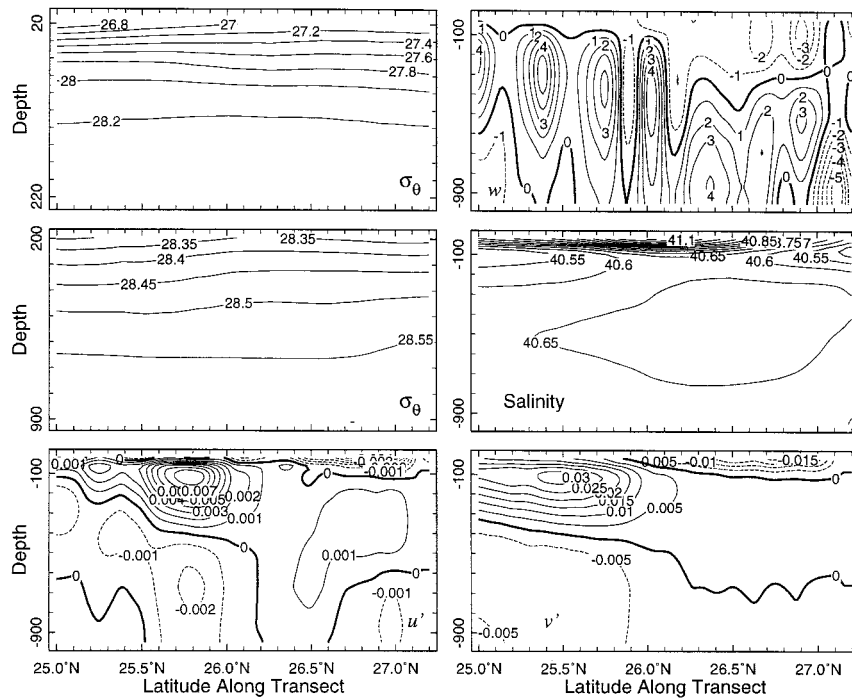


FIG. 26. Sections along the northern western boundary in summer. The properties shown are (left column first, top to bottom):  $\sigma_\theta$  ( $\text{kg m}^{-3}$ , upper 200 m, and 200 to 900 m);  $u'$ , the velocity normal to the transect, positive to the northeast (toward the reader), ( $\text{m s}^{-1}$ ); upwelling ( $\text{m day}^{-1}$ ); salinity (psu); and  $v'$ , the northwestward velocity along the transect ( $\text{m s}^{-1}$ ). This is the summer analog of Fig. 15.

in the summer. Thus, the sea surface positive anomaly along the eastern wall, which drives the northward flowing eastern boundary current, is weaker in summer. The boundary current narrowing is related to a decreased deformation radius  $R$ . The seasonally variable part of  $R$  is  $\Delta\rho h$  (where  $\Delta\rho$  is the density difference between the

mixed layer and the underlying interior and  $h$  is the mixed layer depth). While  $\Delta\rho$  increases in summer,  $h$  decreases considerably. In summer  $\Delta\rho \approx 1.8 \text{ kg m}^{-3}$  and  $h \approx 60 \text{ m}$ , and in winter  $\Delta\rho \approx 0.6 \text{ kg m}^{-3}$  and  $h \approx 400 \text{ m}$ : in summer  $\Delta\rho h$  reduces to less than half of its winter value with the corresponding changes in  $R$ .

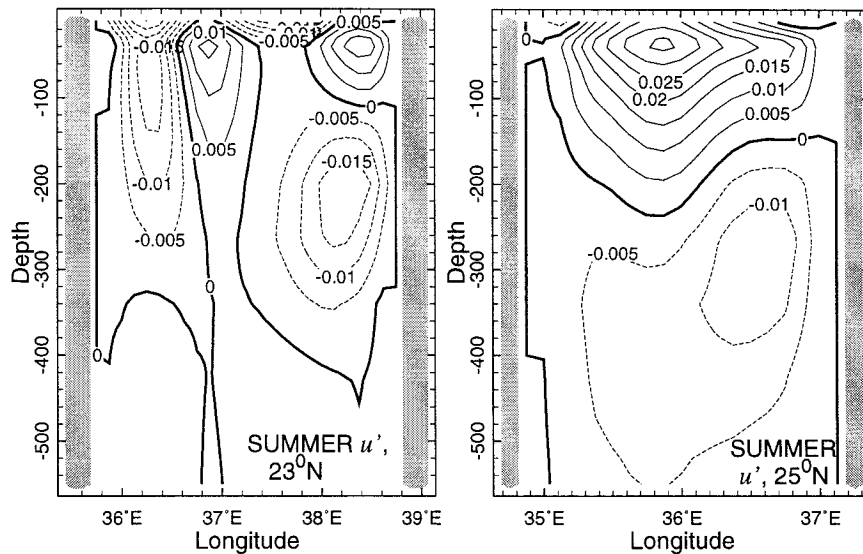


FIG. 27. Summer climatological cross-channel flow; see Fig. 7 for more details.

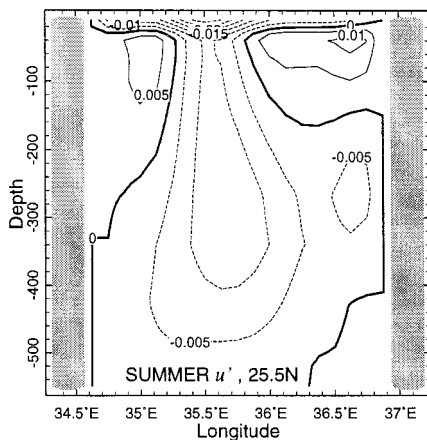


FIG. 28. Summer climatological cross-channel flow at 25.5°N; see Fig. 7 for more details.

Figure 26 shows that the flow speed of the southward flow of eastern boundary current origin is intensified in summer. Near the collision site it is roughly twice as fast as in winter. This is unexpected because of the seasonal reduction of the pressure gradient and all other components of the flow system. The reason for the acceleration is the reduction in  $R$ , which causes the sea-surface elevation difference to occur over a much shorter length scale. The volume flux transported by the current is significantly diminished due to the narrowing and shoaling. The most important message Fig. 26 delivers is that the subduction process does not continue through the summer. The summer downwelling is much shallower and weaker than in winter. It is fragmented in the vertical and horizontal and does not form a coherent structure as in winter. The  $v'$  panel shows that the southward flow along the northern western wall is confined to the upper  $\sim 50$  m. In contrast, the northward flowing western boundary current roughly maintains its depth extent and intensity. The  $u'$  panel shows that, while the western boundary current's departure from the wall continues, some of the flow continues farther north under the surface southward flow. It is clearly different from the winter subduction because the vertical extent of this motion is highly restricted by upwelling below  $\sim 350$  m. The weakened eastward cross-channel leakage of the western boundary current contrasts with the winter situation: because the winter isopycnal doming south of the collision site (due to collision-related subduction) is absent in the summer, the summer flow lacks the winter mass-distribution guidance across the channel.

The convection is about two orders of magnitude less than in winter and is essentially confined to the upper 50 m. As in winter, the summer convection also occurs mostly near the collision site. However, now the convection is not due to sinking, but rather due to the maximum in surface buoyancy loss along the northern western wall (Fig. 9). The haline contribution to the summer total buoyancy loss at the collision site is  $\sim 20\%$ , the

highest in the Red Sea. Earlier we linked this  $E - P$  flux to the conjectural "summer haline preconditioning."

In conclusion, the summer flow does not contain any element that seriously challenges our previously outlined dynamical framework. In fact, the large-scale seasonal differences strengthen and further validate our interpretation. The most important seasonal difference is the shutdown of subduction at the collision site, which we showed is mostly related (directly and indirectly) to the seasonality of the thermodynamic forcing.

## 8. Summary and conclusions

The main finding of this paper is the detailed dynamics of the subductive renewal of the Red Sea upper deep water. Somewhat prophetically, based on tracers data analysis, Cember (1988) first appealed to such a process to resolve apparent discrepancies between distributions of hydrographic properties and those of  $^3\text{He}$ ,  $^{14}\text{C}$ , and other tracers. The subduction takes place slightly south of the northwest corner of the Red Sea. At that point, northward and southward flowing western boundary currents collide, after the one which originally flows to the north along the eastern boundary turns cyclonically, follows the northern boundary, and flows to the south along the western boundary.

We relate the dynamics of the boundary currents to the large-scale sea surface tilt that results from the northward increase of buoyancy loss to the atmosphere. The surface tilt is in geostrophic balance with eastward cross-channel flow. The interactions of the eastward flow with the side boundaries promotes divergence along the western wall and convergence along the eastern wall. The mass distribution that results from these divergence/convergence patterns is consistent with northward flow along both boundaries. It also drives upwelling at the western wall and downwelling at the eastern wall. The vertical motions dominate the vorticity balance through vortex stretching. The vorticity dynamics also accounts for termination of both boundary currents at the collision site. At that point the generation of negative and positive vorticity at the western and eastern walls, respectively, dictates the separation of both currents from the western wall, eastward into the interior. The southward flowing western boundary current is somewhat denser, and thus subducts under the northward flowing one. The process forms deep water when the density of the subducting plume gradually increases through shallow convective interaction with the surface buoyancy loss. We estimate that the rate of deep-water formation (expressed as annually continuous) is 0.11 Sv. Independently, Cember (1988) estimated the flux associated with his "isopycnal mode" is 0.12 Sv.

We speculate that two distinct deep-water formation processes exist, with widely disparate timescales. The haline mode is the regular climatological subduction at

the collision site. Its existence depends on haline preconditioning of the upper-layer water, which occurs throughout the entire northward journey of the surface water from the strait, that is, over a few years. Conversely, the episodic, deep-convective formation is entirely absent from the climatological conditions. It is related to intense atmospheric events and is located at the center of the northern basin cyclonic gyre, where the climatological winter stratification is the weakest. We will pursue this issue in future experiments.

*Acknowledgments.* We are both extremely thankful for Mark Cane's multifaceted, never failing, support. We enthusiastically acknowledge the very helpful comments of two anonymous reviewers; GE gratefully acknowledges the current support of UCAR and NOAA through the Climate and Global Change Postdoctoral Fellowship, and Brian Farrell's hospitality at Harvard.

## REFERENCES

- Basin, S., and G. Reverdin, A note on the equation of state in numerical models of the oceans, unpublished manuscript, Lamont-Doherty Earth Observatory of Columbia University, 1992.
- Cember, R. P., 1988: On the sources, formation, and circulation of Red Sea deep water. *J. Geophys. Res.*, **93**(C7), 8175–8191.
- Chen, D., L. M. Rothstein, and A. J. Busalacchi, 1994: A hybrid vertical mixing scheme and its application to tropical ocean models. *J. Phys. Oceanogr.*, **24**, 2156–2179.
- da Silva, A., C. Young, and S. Levitus, 1994: *Atlas of Surface Marine Data 1994*, Vol. 1: *Algorithms and Procedures*. NOAA Atlas NESDIS, **6**, U.S. Department of Commerce.
- Eshel, G., 1996: Coupling of deep water formation and the general circulation: A case study of the Red Sea. Ph.D. dissertation, Columbia University, 127 pp.
- , M. A. Cane, and M. B. Blumenthal, 1994: Modes of subsurface, intermediate, and deep water renewal in the Red Sea. *J. Geophys. Res.*, **99**(C8), 15 941–15 952.
- Gent, P. R., and M. A. Cane, 1989: A reduced gravity, primitive equation model of the upper equatorial ocean. *J. Comput. Phys.*, **81**, 444–480.
- Hsueh, Y., H. J. Lie, and H. Ichikawa, 1996: On the branching of the Kuroshio west of the Kyushu. *J. Geophys. Res.*, **101**(C2), 3851–3857.
- Huang, R. X., 1991: The three-dimensional structure of the wind-driven gyres: Ventilation and subduction. *Rev. Geophys.*, **29**(Suppl.), 590–609.
- Li, Z., and H. G. Leighton, 1993: Global climatology of the solar radiation budgets at the surface and in the atmosphere from 5 years of ERBE data. *J. Geophys. Res.*, **98**, 4919–4930.
- Maillard, C., 1971: Etude hydrologique et dynamique de la Mer Rouge en hiver. *Ann. Inst. Oceanogr.*, **498**(2), 113–140.
- , and G. Soliman, 1986: Hydrography of the Red Sea and exchanges with the Indian Ocean in summer. *Oceanol. Acta*, **9**(3), 249–269.
- Mantyla, A. W., and J. L. Reid, 1995: On the origins of deep and bottom waters of the Indian Ocean. *J. Geophys. Res.*, **100**(C2), 2417–2439.
- Morcos, S., and G. F. Soliman, 1972: Circulation and deep water formation in the northern Red Sea in winter. *L'Océanographie Physique de la Mer Rouge*, UNESCO, 91–103.
- Murtugudde, R. G., 1993: Upstream finite-difference methods for an isopycnal ocean GCM. Ph.D. dissertation, Columbia University, 174 pp.
- , R. Seager, and A. J. Busalacchi, 1996: Simulation of the tropical oceans with an ocean GCM coupled to an atmospheric mixed layer model. *J. Climate*, **9**, 1795–1815.
- Naik, N., M. A. Cane, S. Basin, and M. Israeli, 1995: A solver for the barotropic mode in the presence of variable topography and islands. *Mon. Wea. Rev.*, **123**, 817–832.
- Oberhuber, J. M., 1988: An atlas based on COADS data set. Tech. Rep. 15, Max-Planck-Institut für Meteorologie Tech. Rep. 15, Hamburg. 121 pp.
- Patzert, W. C., 1972a: Seasonal variations in structure and circulation in the Red Sea. Ph.D. thesis, University of Hawaii at Manoa, 58 pp.
- , 1972b: Seasonal reversal in Red Sea circulation. *L'Océanographie Physique de la mer Rouge*, UNESCO, 55–89.
- Quadfasel, D., and H. Baunder, 1993: Gyre-scale circulation cells in the Red Sea. *Oceanol. Acta*, **16**(3), 221–229.
- Schmitz, W. J., and M. S. McCartney, 1993: On the North Atlantic circulation. *Rev. Geophys.*, **31**, 29–49.
- Seager, R., and M. B. Blumenthal, 1994: Modeling tropical Pacific sea surface temperature with satellite-derived solar radiative forcing. *J. Climate*, **7**, 1943–1957.
- , —, and Y. Kushnir, 1995: An advective atmospheric mixed layer model for ocean modeling purposes. *J. Climate*, **8**, 1951–1964.
- Smith, S. D., 1988: Coefficients for sea surface wind stress, heat flux, and wind profiles as a function of wind speed and temperature. *J. Geophys. Res.*, **93**(C12), 15 467–15 472.
- Trenberth, K. E., 1992: Global analyses from ECMWF and Atlas of 1000 to 10 mb circulation statistics. NCAR Tech. Note 373+STR, National Center for Atmospheric Research, Boulder, CO, 191 pp.